Comparisons of Hybrid En3DVar with 3DVar and EnKF for Radar Data Assimilation: Tests with the 10 May 2010 Oklahoma Tornado Outbreak

Rong Kong[1], Ming Xue[*1,2], Chengsi Liu[1], and Youngsun Jung[1]

[1]*Center for Analysis and Prediction of Storms*
[2]*University of Oklahoma, Norman Oklahoma 73072*

Submitted to Monthly Weather Review
February, 2020
Revised July, September 2020

[*]Corresponding Author: Ming Xue, (mxue@ou.edu), Center for Analysis and Prediction of Storms, 120 David Boren Blvd, Norman OK 73072

Abstract

In this study, a hybrid En3DVar data assimilation (DA) scheme is compared with 3DVar, EnKF, and pure En3DVar for the assimilation of radar data in a real tornadic storm case. Results using hydrometer mixing ratios (CVq) or logarithmic mixing ratios (CVlogq) as the control variables are compared in the variational DA framework. To deal with the lack of radial velocity impact issues when using CVq, a procedure that assimilates reflectivity and radial velocity data in two separate analysis passes is adopted. Comparisons are made in terms of the root mean square innovations (RMSIs) as well as the intensity and structure of the analyzed and forecast storms. For pure En3DVar that uses 100% ensemble covariance, CVlogq and CVq have similar RMSIs in the velocity analyses, but errors grow faster during forecasts when using CVlogq. Introducing static background error covariance **B** at 5% in hybrid En3DVar (with CVlogq) significantly reduces the forecast error growth. Pure En3DVar produces more intense reflectivity analyses than EnKF that more closely match the observations. Hybrid En3DVar with 50% **B** outperforms other weights in terms of the RMSIs and forecasts of updraft helicity, and is thus used in the final comparison with 3DVar and EnKF. The hybrid En3DVar is found to outperform EnKF (3DVar) in better capturing the intensity and structure of the analyzed and forecast storms (intensity and evolution of the rotating updraft).

1. Introduction

The initial conditions are critical for numerical weather prediction (NWP). For convective-scale NWP, when the initial condition does not contain convective-scale information, the model has to go through "spinup" process to develop convective-scale processes that tends to delay the onset of precipitation in the forecast, affecting very-short-range forecast skill of precipitation and other hazardous weather (e.g., Sun et al. 2014). To improve the initial condition and alleviate the spinup problem, efforts assimilating Doppler weather radar observations, including the radial velocity and reflectivity, which contain rich information on precipitating hydrometeors and flow fields within storms, have shown great promises (Sun and Crook 1994; Sun and Crook 1997, 1998; Snyder and Zhang 2003; Xue et al. 2003; Dowell et al. 2004; Tong and Xue 2005; Xue et al. 2006; Tong and Xue 2008; Xue et al. 2009; Yussouf and Stensrud 2010; Auligne et al. 2011; Dawson et al. 2015; Gustafsson et al. 2018). Different data assimilation (DA) methods have been used in these studies.

The three-dimensional variational (3DVar) method is one of the most commonly used DA methods because of the computational efficiency. However, 3DVar is not necessarily best suited for convective-scale DA, because of the lack of simple balance relations at the convective scale among the model state variables, which are often exploited in its large-scale applications (Wu et al. 2002; Sugimoto et al. 2009). The hydrostatic or quasi-geostrophic balances typically assumed for large-scale DA are no longer suitable; instead highly nonlinear 3D dynamics and complex microphysical processes are dominant. Although positive impacts have been found by assimilating radar data using 3DVar (Gao et al. 2004; Xiao et al. 2005; Hu et al. 2006; Xiao et al. 2007; Zhao and Xue 2009; Du et al. 2012; Gao and Stensrud 2012; Ge et al. 2012, 2013; Xue et al. 2014), the assimilation of reflectivity data is often achieved through indirect approaches, such as an add-on complex cloud analysis step (e.g., Hu et al. 2006), latent heat nudging (Wang and T.Warner 1988; Manobianco et al. 1994; Dixon et al. 2009; Ballard et al. 2016; Simonin et al. 2017), or by assimilating pre-retrieved hydrometeor mixing ratios (e.g., Wang et al. 2013). Due to the lack of general balance among the state variables, rapid initial adjustments usually occur in the initial forecasts, leading to rather rapid loss of prediction skill (Kain et al. 2010; Xue et al. 2013).

To produce convective-scale initial conditions in which state variables are dynamically consistent with each other, the NWP model that governs the state evolution should be utilized. The four-dimensional variational (4DVar) method that employs the full NWP model as a strong constraint is a natural choice to fulfill such a requirement; unfortunately, non-linearities associated with complex physical processes that are important for accurate convective scale prediction make the application of 4DVar at the convective-scale technically very challenging. In 2017, hourly cycling 4DVar was implemented at the British Met Office, but radar data assimilation is only limited to radial velocity data (with 15 min DA frequency) (Gustafsson et al. 2018). The application of 4DVar for reflectivity data assimilation has been mainly limited to systems based on simple models (e.g., Sun and Crook 1997).

The ensemble Kalman filter (EnKF, Evensen 1994) is another approach that employs the full NWP model within the DA process through ensemble forecasts; the relations among the state variables are realized through the cross-variable forecast error covariances estimated from the ensemble. Since its initial introduction to convective-scale DA about

15 years ago, the EnKF method has enjoyed great popularity and reasonable success for radar data assimilation and convective scale NWP (e.g., Snyder and Zhang 2003; Dowell et al. 2004; Zhang et al. 2004; Tong and Xue 2005; Xue et al. 2006; Jung et al. 2008; Tong and Xue 2008; Aksoy et al. 2009, 2010; Jung et al. 2010; Dowell et al. 2011; Snook et al. 2011; Zhang et al. 2011; Jung et al. 2012a; Snook et al. 2012; Stensrud et al. 2013).

There are issues with EnKF also, however. Because of the rather limited size of the ensemble that can be afforded in practice, the background error covariance matrix estimated from the limited ensemble is severely rank deficient, which usually leads to spurious long-range correlations (Hamill and Snyder 2000). Although covariance localization helps to alleviate the problem, it usually prevents the inclusion of long-range balances that are physical (Houtekamer et al. 2005; Kepert 2009; Greybush et al. 2011). In comparison, static, non-flow-depedent, climatological background error covariance that often assumes simple Guassian correlation models, is usually full rank, or close to full rank. Certain large-scale/longer-range correlations are often built into the static covariances (e.g., Wu et al. 2002).

To take advantage of the beneficial aspects of static and flow-dependent ensemble covariances, a hybrid approach that utilizes a linear combination or weighted average of the static and ensemble covariances within a 3DVar framework was proposed by Hamill and Snyder (2000), and tested with relatively simple models (Hamill and Snyder 2000; Etherton and Bishop 2004). Lorenc (2003) proposed an alternative computationally much more efficient hybrid algorithm that employs extended control variables, and Wang et al. (2007) showed that this algorithm is mathematically equivalent to that of Hamill and Snyder (2000). The use of hybrid covariances helps alleviate the rank deficiency problem, and allows for the utilization of longer-range correlations found in the static covariance. The use of a variational framework for simultaneous assimilation of all observations enables covariance localization in the model space, instead of the observation space required by EnKF algorithms, such as the ensemble square-root algorithm of Whitaker and Hamill (2002). Also, equation constraints can be incorporated into a variational framework much more easily.

Potential benefits of hybrid DA over 3DVar and EnKF were first demonstrated using the simple models (e.g., Hamill and Snyder 2000; Lorenc 2003; Etherton and Bishop 2004; Wang et al. 2007), then applied to global (Buehner et al. 2010b, 2010a; Clayton et al. 2013) and mesoscale NWP models (e.g., Li et al. 2012; Zhang et al. 2013; Pan et al. 2014). For the convective scales, hybrid DA applications have been more limited; existing studies have only tested the method with simulated observations, assuming no model error (Gao et al. 2013; Gao and Stensrud 2014; Gao et al. 2016; Kong et al. 2018). To apply the hybrid method to radar DA problem, the radar radial velocity and reflectivity data will need to be properly assimilated variationally.

The direct assimilation of reflectivity in a variational framework, however, faces specific difficulties when using the hydrometeor mixing ratios as the control variable (CVq); this is due to the nonlinearity of the reflectivity observation operator, as first reported by Sun and Crook (1997). Specifically, when background rainwater (or snow or graupel or hail) mixing ratio is very small, the gradient of the cost function can become extremely large, making the total cost function minimization difficult to converge. Furthermore, when radial velocity and reflectivity data are assimilated together using CVq, the gradient of the part of cost function related to reflectivity observations is much (orders

of magnitude) larger than that corresponding to radial velocity, making the minimization difficult to converge, and the assimilation of radial velocity data ineffective (Wang and Wang 2016; Liu et al. 2020). Alternatively, indirect assimilation of retrieved rainwater mixing ratio was proposed in Wang et al. (2013) to overcome some of the difficulties, but their study assumed warm-rain processes only, i.e., the reflectivity is only a function of rainwater mixing ratio. Ideally, reflectivity is assimilated directly, and the partitioning among the hydrometeors contributing to the observed reflectivity is left for the DA system to determine. To avoid the same problem, Wang and Wang (2016) proposed to use reflectivity as the control variable instead (referred to as CVZ here). With this approach, tangent linear or adjoint of the reflectivity observation operator is not needed, so that the extremely large values of the tangent linear and adjoint of the observation operator for small mixing ratios can be avoided. However, with the CVZ approach, static background error covariance cannot be easily incorporated into the variational cost function to form a hybrid EnVar system in the traditional sense. This is because that in such a hybrid system, the static background error covariance is unlikely accurate for the highly spatially and temporally varying hydrometeor and reflectivity variables, and as in 3DVar, analysis increments in hydrometeor variables rely almost exclusively on the relationships between hydrometeors and reflectivity as given by the reflectivity observation operator. The adjoint of the operator defines the sensitivity of the hydrometeors to reflectivity, which is used to variationally adjust the hydrometeor state variables given reflectivity observation innovations. Therefore, to effectively include the effect of static background error covariance in a hybrid system, tangent linear and adjoint of the reflectivity observation operator are still needed.

In Carley (2012), the logarithms of the hydrometeor mixing ratios are used as the control variables (named CVlogq hereafter) for radar data assimilation instead of CVq; the use of CVlogq is found to substantially reduce linear approximation errors of the reflectivity observation operator (which is also noted in Wang et al. (2011)) compared to CVq. More recently, Liu et al. (2020) report based on observing system simulation experiments (OSSEs) with 3DVar that CVlogq can avoid the convergence difficulties encountered with CVq, but it can also cause improper spreading of analysis increments when the increment of logarithmic mixing ratios is converted back to mixing ratios. A number of technical treatments were proposed in their study to alleviate the problems, resulting in better analyses and forecasts of a supercell storm. However, the relative performances of CVlogq and CVq for real cases or in an EnVar framework have yet to be examined. As to the special treatments, the following are used. When using CVq, a lower limit is added to the hydrometeor mixing ratios (qLim) or to equivalent reflectivity (ZeLim) in the reflectivity observation operator to confine the gradient of reflectivity DA. A double-pass procedure is used that assimilates reflectivity and radial velocity in two separate passes. When using CVlogq, a smoothing function and a lower limit are applied to the background hydrometeor mixing ratios when converting the analysis increment from the *logq* space back to the *q* space to help suppress improper spreading of the analysis increments. More details can be found in Liu et al. (2020).

In Kong et al. (2018), hybrid ensemble-3DVar (En3DVar) was systematically compared with EnKF, 3DVar, pure En3DVar (with 100% ensemble covariance) in the OSSEs for a simulated supercell storm under perfect model assumption. Radar radial velocity and reflectivity data were assimilated. To facilitate direct comparison between

EnKF and pure En3DVar, a 'deterministic forecast' EnKF algorithm, called DfEnKF, was introduced, in which the ensemble mean forecast within regular EnKF was replaced by a deterministic forecast starting from the ensemble mean analysis making the algorithm more analogous to pure En3DVar. When all algorithms were independently tuned optimally, hybrid En3DVar did not outperform DfEnKF or pure En3DVar, though their analyses were all better than 3DVar analyses. Therefore, when ensemble error covariance was a good estimation of the true error distribution, the benefit of static background error covariance used in the hybrid En3DVar was not obvious in the perfect-model OSSEs. Furthermore, CVlogq or other new treatments developed in Liu et al. (2020) were not used in the OSSEs of Kong et al. (2018). Experiments with real data where model errors are inevitable, and using improved treatments are obviously needed.

In this paper, the hybrid En3DVar algorithm documented in Kong et al. (2018) including additional treatments from Liu et al. (2020) is applied to a real tornadic storm case, and its performance relative to 3DVar, EnKF and pure En3DVar are further examined. The performances of CVq and CVlogq are also compared. We aim to address the following questions for a real case: 1) Does hybrid En3DVar outperform 3DVar and EnKF? 2) Does static **B** have positive contribution to the final analysis and forecasts in the hybrid DA experiments? 3) How different or similar are EnKF and pure En3DVar that uses the same 100% ensemble covariance? 4) How much improvement does the use of CVlogq provide relative to CVq?

The rest of the paper is organized as follows. In section 2, the DA schemes (EnKF, DfEnKF, and hybrid En3DVar) and the observation operators are described. In section 3, the real storm case, the prediction model used, the design of data assimilation experiments, and the radar observations to be assimilated are introduced. In section 4, CVq and CVloq are compared in hybrid En3DVar with different hybrid weights. In addition, EnKF, DfEnKF, and pure En3DVar that use 100% ensemble covariance are compared for the assimilation of reflectivity observations. Sensitivity experiments are conducted to obtain the optimal covariance weights for hybrid En3DVar, using CVq or CVlogq. Finally, hybrid En3DVar with optimal covariance weights, 3DVar, EnKF, DfEnKF are compared based on both objective verifications and subjective evaluations of physical fields. A summary and conclusions are provided in section 5.

2. Data assimilation algorithms and radar observation operators

a. The EnKF algorithm

The ensemble square root filter (EnSRF) algorithm of Whitaker and Hamill (2002), a variant of EnKF, is used, in which the ensemble mean and ensemble perturbations are updated separately:

$$\overline{\mathbf{x}}^a = \overline{\mathbf{x}}^b + \mathbf{K}\left[\mathbf{y} - \overline{H(\mathbf{x}^b)}\right], \tag{1}$$

$$\mathbf{x}_k^{a\prime} = \mathbf{x}_k^{b\prime} - \widetilde{\mathbf{K}}\boldsymbol{H}\left(\boldsymbol{x}_k^{b}\right)'. \tag{2}$$

Here, $\overline{\mathbf{x}}^a = \frac{1}{N}\sum_{k=1}^{N}\mathbf{x}_k^a$ and $\overline{\mathbf{x}}^b = \frac{1}{N}\sum_{k=1}^{N}\mathbf{x}_k^b$ are mean of the ensemble analyses ($\mathbf{x}_k^a$) and background forecast vectors ($\mathbf{x}_k^b$), $\mathbf{x}_k^{b\prime} = \mathbf{x}_k^b - \overline{\mathbf{x}}^b$ and $\mathbf{x}_k^{a\prime} = \mathbf{x}_k^a - \overline{\mathbf{x}}^a$ are the perturbations of ensemble forecasts and analyses. k is index of ensemble member that ranges from 1 to

ensemble size N. $\mathbf{y}$ is the observation vector. H is the observation operator which can be nonlinear. Here,

$$\mathbf{K} = \left[\rho_s \circ \left(\hat{\mathbf{P}}^{\mathrm{b}}\mathbf{H}^{\mathrm{T}}\right)\right]\left(\mathbf{H}\hat{\mathbf{P}}^{\mathbf{b}}\mathbf{H}^{\mathbf{T}} + \mathbf{R}\right)^{-1}, \tag{3}$$

$$\widetilde{\mathbf{K}} = \left(1 + \sqrt{\frac{\mathbf{R}}{\mathbf{H}\hat{\mathbf{P}}^{\mathbf{b}}\mathbf{H}^{\mathbf{T}}+\mathbf{R}}}\right)\mathbf{K}. \tag{4}$$

$\mathbf{K}$ ($\widetilde{\mathbf{K}}$) is the ("reduced") Kalman gain, $\mathbf{H}$ is the tangent linear observation operator. Ensemble covariance $\hat{\mathbf{P}}^{\mathrm{b}}$ is estimated from $\mathbf{x}_k^b$ and used in the Kalman gain. $\mathbf{R}$ is the observational error covariance. A Gaspari and Cohn (1999) localization function is used to localize the ensemble covariance; $\rho_s \circ$ is the Schur product with the correlation matrix ρ_s. A more detailed description on the EnSRF algorithm as implemented in the Advanced Regional Prediction System (ARPS) framework can be found in Xue et al. (2006) and Kong et al. (2018).

b. The DfEnKF algorithm

In the standard EnKF, as in Eq. (1) of EnSRF, the ensemble mean analysis $\overline{\mathbf{x}}^a$ is based on the ensemble mean forecast $\overline{\mathbf{x}}^b$ and its observational counterpart $\overline{H(\mathbf{x}^b)}$. However, in En3DVar, a single, deterministic forecast is run from the En3DVar analysis of the previous cycle, and this forecast is updated by the En3DVar algorithm. To facilitate more direct comparison between EnKF and En3DVar, an alternative implementation of EnKF, called DfEnKF, first introduced by Kong et al. (2018), is also tested here. In DfEnKF, a single deterministic forecast $\mathbf{x}_d^f$, serving as the background $\mathbf{x}_d^b$, that starts from a previous analysis $\mathbf{x}_d^a$, is updated using the ensemble mean update equation given in (1). To better describe the algorithm, Eq. (6) in Kong et al. (2018) is reproduced here:

$$\mathbf{x}_d^a = \mathbf{x}_d^b + \mathbf{K}\left[\mathbf{y} - H\left(\mathbf{x}_d^b\right)\right], \tag{5}$$

where $\mathbf{x}_d^a$ is the DfEnKF analysis, $\mathbf{x}_d^b$ is from the deterministic forecast $\mathbf{x}_d^f$ at the beginning of the analysis cycle, and $\mathbf{K}$ is the same Kalman gain as in Eq. (1). This 'deterministic' analysis in Eq. (5) is run at the same time as the ensemble mean analysis in Eq. (1), just like the En3DVar analysis is run alongside the EnKF. When 100% ensemble covariance derived from the ensemble perturbations from the EnKF system is used in En3DVar, its solution should be theoretically the same as the solution of Eq. (5), under idealized conditions. More discussions on this algorithm can be found in (Kong et al. 2018).

c. The 3DVar and En3DVar algorithms

The hybrid En3DVar algorithm follows Lorenc (2003), in which the flow-dependent ensemble covariance is introduced into a 3DVar framework via a set of extended control variables (Liu and Xue 2016). Within hybrid En3DVar, the background error covariance is effectively a weighted average of the static and flow-dependent ensemble covariances, and the weights vary between 0 and 1; when the weight of static error covariance is 1 (0), the scheme becomes pure 3DVar (pure En3DVar). Detailed equations of the En3DVar algorithm as well as information on the radar radial velocity and reflectivity observation

operators can be found in (Kong et al. 2018). To produce physically consistent hydrometeor analyses, temperature-dependent vertical profiles are specified for the static background errors of hydrometeor variables in 3DVar and hybrid En3DVar based on Liu et al. (2019). Because of the lack of cross-covariance in the static background error covariance, the 3DVar is by itself univariate although additional equation constraint in the cost function can couple state variables together. Spatial covariance is realized through spatial recursive filter (Gao et al. 2004).

3. Case overview, prediction model, and DA experiment design

a. Case overview

On 10 May 2010, a total of 56 tornadoes favored by an intense dry line occurred in the state of Oklahoma, including two intensity level 4 on the enhanced Fujita scale (EF4, WSEC 2006) and four intensity level 3 on the enhanced Fujita scale (EF3) tornados that produced significant damage over many areas. Three people were killed and over 450 people were injured in the state of Oklahoma during the tornado outbreak. This was the second largest tornado outbreak documented in Oklahoma (with the largest one occurring on May 3, 1999). From 1700 to 1941 CDT, a total of 42 different tornadoes occurred. The tornadic storms moved at speeds of 50 to 60 miles per hour, with the tornado damage paths spreading over a north-south area of over 200 miles; softball size (about 3.5 inches in diameter) hail was also reported at several locations.

According to the National Weather Services, there were 13 different storms producing tornadoes on that day. They are denoted storms A through O (see https://www.weather.gov/oun/events-20100510). Among these storms, storm J was the most productive, spawning 20 out of 55 tornadoes, including one EF4 (J1) and one EF3 (J4) tornado, causing one fatality and several injuries. Considering that tornado J4 (referred to as the Seminole storm hereafter since most of the damage path is located in Seminole county, Fig. 1) has the largest damage width, the convective system that spawned tornado J4 is selected as the focus system of this study.

b. Prediction model

The ARPS model is used during the DA cycles and the free forecasts after DA. To capture all long track storms traversing Oklahoma that day, the model domain is set to cover most Oklahoma except for its northwest panhandle area (the narrow westward extension of the State of Oklahoma that looks like a handle of a frying pan), centering at 35.7°N and 97.5°W (Fig. 1). The domain size is 363 × 363 × 53, with a 1 km grid spacing in the horizontal and 0.4 km on average in the vertical with vertical grid stretching. The minimum vertical grid spacing near the surface is 20 m. Full model physics are used, including the 1.5-order turbulent kinetic energy (TKE)-based subgrid-scale turbulence parameterization (Sun and Chang 1986), a two-layer soil model (Noilhan and Planton 1989), and the Lin et al. (1983) single-moment ice microphysics. More details on the physics options can be found in Xue et al. (2001). Forth-order monotonic computational mixing is used to help suppress grid-scale noise. The values of intercept parameters for rain, snow, and hail used are 8×10^6 m^{-4}, 3×10^6 m^{-4}, and 4×10^4 m^{-4}, respectively, in both the microphysics scheme and the reflectivity operator.

c. Design of assimilation experiments

The initial ensembles with a 1-km grid spacing are interpolated from a set of parent (40-member) ensemble analyses at 1900 UTC 10 May 2010 that are initialized at 1500 UTC and assimilate surface, upper-air, profiler, and radar observations with a 4-km grid spacing using the ARPS EnKF (Jung et al. 2012b; Jung et al. 2013). Similarly, the external boundary conditions (also with a 4-km grid spacing) are interpolated from the hourly parent ensemble forecasts initialized from the parent ensemble analyses at 1500 UTC using the ARPS model (Xue et al. 2000; Xue et al. 2001). Since the ensemble is initialized from coarser-resolution analyses, 30-minute spin-up ensemble forecasts are first run from 2100 UTC on the 1-km experiment grid. Radar radial velocity and reflectivity data from radar sites in Oklahoma (KTLX, KINX, KVNX, KFDR) are then assimilated every 5 minutes from 2130 UTC to 2230 UTC using 3DVar, EnKF/DfEnKF, and En3DVar with and without static covariance (corresponding to hybrid and pure En3DVar, respectively) DA methods (Fig. 2). Multiplicative inflation with an inflation factor of 20% is applied to regions where observed reflectivity is higher than 5 dBZ. In addition, adaptive inflation that inflates the posterior ensemble spread in proportion to the amount of ensemble spread reduced in DA (Whitaker and Hamill 2012) is applied. The inflation coefficient used is 0.95. Covariance localization radii for radar observations are set to 6 km and 4 km in horizontal and vertical directions, respectively, using a fifth-order correlation function of Gaspari and Cohn (1999). Similar radii are used in Snyder and Zhang (2003) and Aksoy et al. (2009) For pure and hybrid En3DVar, the recursive filter decorrelation length scales for the localization of ensemble covariance are 1.6 km in the horizontal and 1.1 km in the vertical respectively, which are equivalent to the 6 km and 4 km cutoff radii for EnKF based on Eq. (4) in Pan et al. (2014). For 3DVar, the decorrelation scales for the static background error covariance used are 4.1 km and 1.4 km in horizontal and vertical directions, respectively, following those used in (Kong et al. 2018).

Radar data assimilated are radial velocity where observed reflectivity exceeds 10 dBZ, and reflectivity data everywhere (including 'clear-air' reflectivity, e.g., reflectivity <5 dBZ) from four WSR-88D radars (Oklahoma City, Tulsa, Vance Air Force Base, and Frederick or KTLX, KINX, KVNX, KFDR). The observation errors for reflectivity and radial velocity are 5 dBZ and 3 m s^{-1}, typical of expected errors with real radar observations that also include representation errors.

Five experiments are performed to evaluate the performance of different DA algorithms, i.e., hybrid En3DVar, pure En3DVar, 3DVar, EnKF, and DfEnKF. As defined in Kong et al. (2018), DfEnKF is updated in the same manner as the ensemble mean background in EnKF and, therefore, is algorithm-wise parallel to pure En3DVar. At the end of DA cycles at 2230 UTC, a single deterministic forecast is launched from the ensemble mean or deterministic analysis of each algorithm. The configurations of these experiments are summarized in Table 1.

In EnKF and En3DVar DA, we choose not to update the horizontal velocity fields (u, v) using assimilating reflectivity data because the relatively small physical correlations among their background forecast errors can be dominated by noise/errors, leading to large errors in analyzed winds if updated (by reflectivity). A weight of 5 %, 25 %, 50 %, and 75 % are given to the static background error covariance (experiments names are suffixed with "%B" in Table 1) in a set of hybrid En3DVar sensitivity experiments, and the results are compared to determine the optimal covariance weights.

As discussed in Introduction, the gradient of the cost function of reflectivity can be much larger than that of radial velocity when hydrometeor mixing ratios are used as the control variables and, thus, radial velocity assimilation becomes ineffective (Wang and Wang 2016; Liu et al. 2020). We compare two experimental setups: 1) directly using hydrometeors as the control variables (CVq), but assimilating reflectivity and radial velocity data separately in two passes (corresponding experiments using a single pass are also done but the results are clearly worse and therefore not included); 2) using logarithmic mixing ratios as the control variables (CVlogq) and assimilating radial velocity and reflectivity data together. The performances of CVq with double passes and CVlogq are evaluated in the En3DVar framework, using different hybrid covariance weights. The results of different DA experiments are compared. More details on the experiments can be found in Table 1.

d. Radar data preprocessing and quality control

The operational WSR-88D radar data from four radar sites in Oklahoma (KTLX, KINX, KVNX, KFDR) are interpolated horizontally to the ARPS model grid column locations but are kept on the original radar elevation levels in the vertical. A radar beam-pattern weighting function is applied in the vertical in the radial velocity and reflectivity observation operators, as described in Xue et al. (2006). Automatic quality control is applied to the radar data that includes velocity dealiasing, despeckling, and removal of ground clutters and anomalous propagation artifacts (Brewster et al. 2005).

4. Results of assimilation experiments

a. Comparisons between CVq and CVlogq with hybrid En3DVar and different weights

The root mean square innovation (RMSI, where innovation is the difference of observation prior or posterior from observation) is used to quantify model analysis and forecast quality and compare the performance of different DA algorithms. In this study, the RMSIs are calculated over regions where the observed reflectivity exceeds 15 dBZ. Figure 3 shows the RMSIs of radial velocity and reflectivity analyses and forecasts from hybrid En3DVar with different weights of static covariance **B** using CVq or CVlogq. For hybrid En3DVar with 0% static **B**, CVq and CVlogq exhibit similar innovations (or loosely speaking, errors) in analyzed radial velocity and reflectivity (Figs. 3a, b) but the forecast error growth is noticeably faster with CVlogq especially for radial velocity, suggesting more balanced analyses among the state variables using CVq (Figs. 3a, b) in this case with 0% **B**. We note here, as was done in Pan et al. (2014), that for an En3DVar system coupled with an EnKF system that provides the ensemble covariance, the EnKF system should in principle also use two separate passes if two passes are used by En3DVar (with CVq), assimilating the same set of observations in each pass. This is not done here, because doing so will significantly increase the computational cost, and it is our goal to show that using CVlogq can produce quality analyses without resorting to the two-pass procedure. The fact that for the second pass of En3DVar (with CVq) that assimilates Vr observations, the ensemble perturbations are not updated as they should be after Z observations are assimilated would tend to allow Vr data to have larger impacts on the state variables that are updated by them (due to the lack of reduction in the ensemble spread by Z earlier); this may explain why CVq which uses two passes, appears to be more effective in producing more balanced analyses and more accurate forecasts.

Introducing non-zero **B** into En3DVar significantly improves the fit of analyzed V_r to observations in all experiment as evidenced by the smaller RMSIs of analysis in Figs. 3c, 3e, 3g, 3i, and 3k; the analysis RMSIs for Vr are smallest for CVlogq with 50% **B** (Fig. 3g). During the analysis cycles, the Vr forecast errors increase when more weights are given to **B** for both CVlogq and CVq, while the improvement to Z RMSIs due to non-zero **B** is mostly limited to Z forecasts for CVlogq (e.g., Figs. 3f - 3l). During the free forecast period, the largest improvement is seen in the CVlogq experiments, where the Vr RMSIs become similar to those of CVq cases, and the Vr forecast RMSIs are slightly lower with non-zero **B** after the first 10 minutes of forecast (left column of Fig. 3), and those of CVlogq are slightly larger after 40 minutes of forecast. For Z forecast RMSIs, those of CVlogq become more noticeably lower than those of CVq after the first 20 minutes of free forecast for 25% or more weight of **B** (e.g., Fig. 3f).

Since CVq requires that reflectivity and radial velocity data are assimilated separately in two separate passes to achieve similar performance as CVlogq, it is computationally more expensive. Also, since the static or ensemble background error covariance is not updated across the passes, the use of multiple passes is theoretically problematic. If the EnKF has to be split into two passes, the increase in computational cost will be much more, making the approach unsuitable for operational use. For these reasons, and the fact that the Z forecast RMSIs are somewhat lower in later forecasts, CVlogq will be used in the En3DVar experiments in the rest of this paper.

b. Comparisons between EnKF, DfEnKF, and pure En3DVar for reflectivity DA

EnKF, DfEnKF, and pure En3DVar (PEn3DVar) all use 100% ensemble covariances. In theory, they should produce similar results, at least under idealized conditions including linearity and the absence of sampling error. In practice, their performances can be different, especially when the observation operator (such as that of Z) is highly nonlinear as shown by Kong et al. (2018) in perfect model OSSEs. In this section, we compare the performance of these three algorithms for a real case, assimilating reflectivity observations only (because the algorithms tend to differ more when assimilating reflectivity whose observation operator is nonlinear). As discussed earlier and in Kong et al. (2018), DfEnKF, being a deterministic algorithm, is more analogous to PEn3DVar.

The RMSIs of the analyzed Z from experiments EnKF, DfEnKF and PEn3DVar (Table 1 for CVlogq experiments) are plotted every 15 min in Fig. 4, together with those of CTRL for reference. Compared to CTRL, all three DA experiments significantly reduce the RMSIs of Z analyses. EnKF and DfEnKF perform very similarly and both have a few percent higher RMSIs than PEn3DVar (Fig. 4).

To see why PEn3DVar has smaller RMSIs than EnKF (or DfEnKF), the analyzed Z at 8 km (where differences are most obvious) above ground level (AGL) for the first four analysis cycles are depicted in Fig. 5. The overall structures of analyzed Z in EnKF and DfEnKF are similar and both underestimate the intensity of Z compared to PEn3DVar and the observations in the earlier cycles. After the third cycle, the analyzed Z of EnKF, DfEnKF, and PEn3DVar become similar. As discussed in Kong et al. (2018), the serial (where observations are assimilated one by one in EnKF and DfEnKF) versus global (where all observations are assimilated simultaneously in PEn3DVar) nature and the direct updating of state variables using the filter equations (in EnKF and DfEnKF) versus variational minimization to find the analysis increments (in PEn3DVar) can cause differences in the analysis results. With the EnKF algorithm that is serial, when significant

under dispersion occurs during the DA processes, observations assimilated later in the serial data processing (within the same cycle) may have too small impact, and the global En3DVar algorithm may have advantage. However, the RMSI differences between EnKF/DfEnKF and PEn3Dvar for this case are probably not statistically significant.

c. Optimal covariance weights for hybrid En3DVar

To determine a relative 'optimal' weight for hybrid En3DVar, four sets of experiments are selected from section 4a, which are experiments with 5%, 25%, 50%, and 75% static background error covariance **B** with CVlogq. The corresponding experiments are named as HEn3DVar5%B, HEn3DVar25%B, HEn3DVar50%B, and HEn3DVar75%B, respectively (Table 1). Their results are also compared with PEn3DVar and 3DVar that are effectively hybrid algorithms using 0% and 100% static **B**, respectively.

The Z analyses after 1-h DA are very close, as evidenced by similar RMSIs at 2230 UTC (Figs. 3d, 3f, 3h, 3j, 3l). When comparing the Z fields at 1 km AGL after 45 minutes of forecast, the Z forecasts from hybrid En3DVar with weights of **B** higher than 25% are similar to or better than those of lower weights in capturing the Z intensity and structure of the main supercell compared to the observations (Fig. 6). Storms in HEn3DVar5%B (Fig. 6b), especially the main tornadic supercell storm with a clear hook echo (Fig. 6a), are less organized than those in experiments with 25 to 75% **B**. The subjective evaluations based on the structures of Z forecasts are consistent with the RMSIs of Z forecasts shown in Fig. 3; the RMSIs for hybrid CVlogq experiments are lower in later forecasts for **B** weights larger than 25%. Combined with the fact that the Vr analysis RMSIs are lowest with 50% **B** (Fig. 3g), equal weights for the static and ensemble covariances appear to be optimal. This is in contrast to the results of perfect model OSSEs of Kong et al. (2018), where the benefit of including static background error covariance **B** is not obvious. We believe that when the prediction model is perfect, the state estimation and ensemble covariances can be rather accurate, as found in Tong and Xue (2005), the inclusion of a static **B** is not necessary. In our current real case, model error is inevitable, and significant errors tend to exist in both analyses and forecasts, the benefit of including static **B** is more obvious, and the optimal weight assigned to the static **B** is actually quite large at 50%. As shown in Fig. 6, the storms west of the major line of storms that have developed during the forecast period along a dry line are mostly missed in all experiments. To improve the forecast of these storms, observations that can help improve the pre-storm environment near the dryline are likely needed (Xue and Martin 2006; Liu and Xue 2008).

As described earlier in the case overview, the May 10, 2010 case is one with multiple tornadoes. During the current forecast period, the observed supercell storm over Pottawatomie and Seminole counties produced an EF3 tornado (J4 in Fig. 1). To see how well the predicted storm over that region is capturing supercell storm characteristics, in particular a rotating updraft, among the hybrid En3DVar DA experiments, we plot the accumulated swaths of the 2 – 5 km integrated updraft helicity (UH, Kain et al. 2008) that are greater than 200 $m^2 s^{-2}$ during the 0 – 1.5 h forecast period, along with the observed J4 tornado damage path (Fig. 7). The swath of predicted UH in convection-allowing models has been shown to be a good predictor of tornado potential and is often used to evaluate prediction of tornadic supercell storms (e.g., Clark et al. 2013; Snook et al. 2019; Stratman et al. 2020).

As shown in Fig. 7, the strongest forecast UH swath is off to the southeast of the observed tornado track with 5 % **B** (Figs. 7a), and the swaths are also much weaker than in

other experiments (Fig. 7). When the weight of static **B** is equal to or greater than 25 %, the swath of the most intense UH is collocated with the observed tornado damage path. Among these experiments, HEn3DVar50%B and HEn3DVar75%B have stronger and more focused (narrower) UH swaths that cover the observed tornado damage path (Figs. 7c and 7d). Combined with earlier discussions, we choose again 50 % as the optimal weight for static **B** for the hybrid En3DVar.

d. Comparisons of EnKF, DfEnKF, 3DVar, and hybrid En3DVar with optimal weights

With the optimal weight of **B** at 50% in HEn3DVar50%B, the RMSIs of Vr and Z analyses and forecasts are compared with those of CTRL, EnKF, DfEnKF and 3DVar in Fig. 8. Compared to CTRL, all DA experiments are able to reduce the RMSIs. The velocity forecasts of EnKF during the DA cycles have much smaller RMSIs than other DA experiments (including DfEnKF, Fig. 8a). Much of this difference is actually because of the effects of ensemble averaging to arrive at the ensemble forecasts used to calculate the Vr RMSIs. The wind fields in the deterministic forecasts used to calculate RMSI in all other experiments tend to contain a lot finer scale structures that are difficult to match up with those in the Vr observations while the ensemble averaging smooths out many of the smallest-scale structures. During the free forecast, EnKF initially benefits from the reduced level of analysis RMSI, but later its RMSIs become close to those of other DA experiments. All free forecasts are single deterministic forecasts. The Vr RMSIs for HEn3DVar50%B, 3DVar, and DfEnKF have similar levels for both velocity analyses and forecasts, with those of DfEnKF forecasts being slightly larger up to 20 min into the free forecast.

For Z, the RMSIs for both analyses and forecast within the DA cycles, are, however, a lot closer between EnKF and DfEnKF (Fig. 8b), presumably because the Z fields contain less fine-scale structures than the wind fields so that ensemble mean for DfEnKF does not have as much impact. During the free forecast period, the DfEnKF Z RMSIs are initially larger but become smaller after 15 min compared to those of EnKF. For reflectivity, the RMSIs for 3DVar and HEn3DVar50%B are very similar within the DA cycles and throughout the free forecast period (Fig. 8b), and are consistently lower than those of EnKF and DfEnKF, suggesting that the variational algorithms, 3DVar and hybrid En3DVar, outperform the EnKF algorithms, in terms of Z. As discussed earlier, and in Kong et al. (2018), the nonlinearity in the reflectivity operator tends to make a difference between the global variational algorithms and the serial EnKF algorithms. It is somewhat surprising, however, that 3DVar performs almost as well as the hybrid En3DVar algorithm with optimal hybrid weights, given that 3DVar does not contain any cross-variable covariance. The results are generally consistent with the results in Fig. 3, where the CVlogq hybrid En3DVar results are similar once the weight of static B is 25% or higher. It appears that for this real case, the quality of ensemble-derived covariance is not that good so that the analyses can benefit from a significant fraction of static **B** even though it lacks cross-covariances. During the short, rapid assimilation cycles, state variables not directly updated by 3DVar much have been adjusting quickly to variables better constrained by the Vr and Z observations.

Figure 9 compares 45-min forecast Z from different experiments, at the time when the Seminole tornadic storm was most intense in terms of Z during the free forecasts. HEn3DVar50%B and 3DVar are able to forecast an intense supercell storm near the location of observed Seminole storm. The forecast storm in pure En3DVar (PEn3DVar) does not have a clearly defined hook echo (Fig. 9e) while EnKF significantly

underestimates Z intensity and coverage of the supercell storm. DfEnKF predicts the storm coverage better than EnKF and PEn3DVar but still underestimates the intensity. The hook echo signature of the tornadic supercell storm is better captured in 3DVar and HEn3DVar50%B, with that in the latter being better defined.

Figure 10 compares the 2 – 5 km UH (greater than 200 $m^2 s^{-2}$) swaths of 0 –1.5 h free forecasts (after DA) for each experiment against the J4 tornado damage path. The intensity of UH forecasts from EnKF and PEn3DVar are much weaker than other DA experiments (Figs. 10a, d). DfEnKF is able to produce a long and intense UH swath but places too far north (Fig. 10b). On the other hand, the locations of the UH swath from 3DVar and HEn3DVar50%B compare well with the tornado damage path. However, the intensity of storm rotations near the end of the damage path (forecasts) weakens too early in 3DVar, while high UH (>1400 $m^2 s^{-2}$) values are maintained throughout the entire J4 tornado period in HEn3DVar forecasts (Fig. 10e).

To better compare the forecast wind structure among the DA experiments, we plot in Fig. 11 the 1-h forecast V_r at the lowest elevation angle from different experiments, we see that HEn3DVar50% better captures the velocity couplet associated with the mesocyclone within the supercell than other experiments (Fig. 11). The results are consistent with the higher intensity of the 1-h UH forecasts (pointed by black arrows in Figs. 10c, e) from hybrid En3DVar than that from 3DVar as well as the others.

To understand the reasons for the performance difference in the forecasts, surface perturbation potential temperature fields from DfEnKF, 3DVar and HEn3DVar50%B are compared (Fig. 12). The fields from different experiments after 1-h DA are similar (Fig. 12 a-c). However, the forecast cold pool (especially at 60 min of forecast) from 3DVar is colder than the other two cases (Fig. 12 d - i). As shown in Fig. 11, HEn3DVar50% better captures the velocity couplet associated with the mesocyclone within the supercell than 3DVar, which is believed to be related to the weaker cold pool of HEn3DVar50%B relative to that of 3DVar. Tornadogenesis is more likely in supercells that have intermediate intensity cold pools rather than too strong or too weak cold pools (Markowski et al. 2002; Grzych et al. 2007; Hirth et al. 2008; Markowski and Richardson 2014).

A convective cold pool is usually related to melting of ice particles and evaporation of rain water at the lower levels. The vertical cross-sections of the mixing ratios of rainwater and hail through the maximum vertical velocities of DfEnKF, 3DVar, and HEn3DVar50%B are compared in Fig. 13. The mixing ratios of the hail and rainwater at the lower levels from 3DVar is much larger than those of the others in the forecasts after DA (Fig. 13), indicative of the potential for more hail melting and rainwater evaporation and thus more intense cold pool in the forecasts of 3DVar.

The vertical cross-sections of the vertical velocity fields from DfEnKF, 3DVar, and HEn3DVar50%B are compared in Fig. 14. The updraft from 3DVar is weaker than that of HEn3DVar50%B, likely leading to more rainwater and hail falling to the low levels and thus more intense cold pool. Overall, the reason that HEn3DVar50%B has better performance than 3DVar is likely because that En3DVar produces analyzed state variables that are more physically consistent with each other and so that the analyzed storm can be sustained in the forecast and hydrometeors do not fall to ground too quickly. The analyzed hydrometeor mixing ratios from DfEnKF are the smallest (Fig. 14a), which appears to explain why the weakest updraft in DfEnKF does not lead to a strong cold pool in the forecasts (Fig. 12a).

5. Summary and conclusions

In this study, radar data from 4 operational WSR-88D radars are assimilated using hybrid En3DVar, 3DVar, EnKF, and pure En3DVar schemes and their relative performance is compared for the 10 May 2010 Oklahoma severe storms including a tornadic supercell. Radar radial velocity and reflectivity data are assimilated every 5 minutes for 1 hour followed by 1-hour ensemble and deterministic forecasts. To alleviate the unique difficulties assimilating radar reflectivity and radial velocity together in the variational framework, two alternative approaches are taken here: 1) use hydrometeor mixing ratios as the control variables (CVq), but assimilate reflectivity and radial velocity data in two separate analysis passes and 2) use logarithmic hydrometeor mixing ratios as the control variables (CVlogq) and assimilate reflectivity and radial velocity simultaneously. CVq and CVlogq are compared in the pure En3DVar and hybrid En3DVar frameworks. In addition, EnKF is compared with pure En3DVar that uses 100% ensemble covariance. To facilitate direct comparison between EnKF and pure En3DVar, results using a deterministic forecast EnKF (denoted DfEnKF) introduced in Kong et al. (2018) is also included here. Finally, Hybrid En3DVar with 5 %, 25 %, 50 %, and 75 % weight of static background error covariance **B** is compared with 3DVar, EnKF, DfEnKF, and pure En3DVar in terms of RMSIs and subjective assessment of storm features. The experiment results and related conclusions are summarized as follows:

- Pure En3DVar with CVlogq and CVq have similar RMSIs in radial velocity analyses but the error growth rate is much larger in CVlogq than in CVq, suggesting CVq analysis is more balanced than that of CVlogq. However, the large error growth in CVlogq is significantly reduced by introducing a small percentage (e.g., 5%) of static **B** in hybrid En3DVar. Since CVq requires reflectivity and radial velocity data being assimilated separately in two passes to achieve similar performance to CVlogq, En3DVar with CVlogq is preferred over the use of the CVq approach, although pure En3DVar with CVlogq produces somewhat larger RMSIs of radial velocity than CVq.
- EnKF and DfEnKF perform similarly and both underestimate the intensity of the reflectivity analyses compared to pure En3DVar analyses, especially in the earlier cycles.
- Hybrid En3DVar with four different weights (5 %, 25 %, 50 %, 75 %) of static **B** are compared in terms of the RMSIs as well as forecasts of storm updraft helicity (UH) to determine an optimal choice of weight among them. They are also compared with pure En3DVar and 3DVar that effectively have 0% and 100% weight of **B**. Hybrid En3DVar with 50% of **B** is found to perform better than other weights; it better captures the hook echo structure of the major tornadic supercell storm in the 45 min forecast of reflectivity, as well as in 0 – 1 h forecasts of UH.
- Hybrid En3DVar with 50% **B** is compared with 3DVar, EnKF, DfEnKF, and pure En3DVar in terms of RMSIs and analyses/forecasts of storm intensity/structures. 3DVar and hybrid En3DVar outperform EnKF and DfEnKF in terms of the intensity and structure of storm analyses and forecasts. The intensity and evolution of UH forecasts are better depicted in hybrid En3DVar relative to 3DVar. The RMSIs of radial velocity forecasts during the DA cycles from EnKF is much smaller than those of DfEnKF and En3DVar in which a single deterministic forecast instead of the ensemble mean forecast is used as the forecast background

for the analysis. Such a difference suggests that the averaging of wind forecasts (wind fields tend to have more special scale structures) over ensemble members help decrease errors in the ensemble mean velocity forecasts (which are used to calculate the RMSIs).

- The better forecast resulting from hybrid En3DVar appears to be due to its more physically consistent state variables analyzed that can better sustain the storms in the forecast.

Finally, we note that the conclusions obtained here are based on a single real data case. As first paper to perform such detailed comparisons for real storms, we believe such a study is necessary and allows for more detailed examination of the assimilation and forecast results. More storm cases are obviously needed to further examine the relative performance of hybrid En3DVar, pure 3DVar, and EnKF, to further optimize the algorithms, and to draw more reliable and general conclusions. This is planned for future studies.

Acknowledgements. This research was primarily supported by the NOAA Wan-on-Forecast (WoF) Grant NA16OAR4320115. The second author was also supported by NSF Grants AGS-0941491 and AGS-1046171. Computing was performed primarily on the XSEDE Stampede2 and comet supercomputer at the University of Texas Advanced Computing Center (TACC) and the Oklahoma Super-computing Center for Research and Education (OSCER).

References

Aksoy, A., D. C. Dowell, and C. Snyder, 2009: A Multicase Comparative Assessment of the Ensemble Kalman Filter for Assimilation of Radar Observations. Part I: Storm-Scale Analyses. *Mon. Wea. Rev.*, **137,** 1805-1824.

——, 2010: A Multicase Comparative Assessment of the Ensemble Kalman Filter for Assimilation of Radar Observations. Part II: Short-Range Ensemble Forecasts. *Mon. Wea. Rev.*, **138,** 1273-1292.

Auligne, T., A. Lorenc, Y. Michel, T. Montmerle, A. Jones, M. Hu, and J. Dudhia, 2011: Toward a New Cloud Analysis and Prediction System. *Bull. Amer. Meteor. Soc.*, **92,** 207-210.

Ballard, S. P., Z.Li, D.Simonin, and J.-F.Caron, 2016: Performance of 4D-Var NWP-based nowcasting of precipitation at the Met Office for summer 2012. *Quart. J. Roy. Meteor. Soc.*, **142,** 472–487.

Brewster, K., Ming Hu, Ming Xue, and Jidong Gao, 2005: Efficient assimilation of radar data at high resolution for short-range numerical weather prediction. *WWRP Int. Symp. Nowcasting Very Short Range Forecasting***,** CDROM 3.06.

Buehner, M., P. L. Houtekamer, C. Charette, H. L. Mitchell, and B. He, 2010a: Intercomparison of Variational Data Assimilation and the Ensemble Kalman Filter for Global Deterministic NWP. Part I: Description and Single-Observation Experiments. *Mon. Wea. Rev.*, **138,** 1550-1566.

——, 2010b: Intercomparison of Variational Data Assimilation and the Ensemble Kalman Filter for Global Deterministic NWP. Part II: One-Month Experiments with Real Observations. *Mon. Wea. Rev.*, **138,** 1567-1586.

Carley, J. R., 2012: Hybrid ensemble-3DVar radar data assimilation for the short-term prediction of convective storms.**,** 205 pp.

Clark, A. J., and Coauthors, 2013: Tornado Pathlength Forecasts from 2010 to 2011 Using Ensemble Updraft Helicity. *Wea. Forecasting*, **28,** 387-407.

Clayton, A. M., A. C. Lorenc, and D. M. Barker, 2013: Operational implementation of a hybrid ensemble/4D-Var global data assimilation system at the Met Office. *Quart. J. Roy. Met. Soc.*, **139,** 1445-1461.

Dawson, D. T., M. Xue, J. A. Milbrandt, and A. Shapiro, 2015: Sensitivity of Real-Data Simulations of the 3 May 1999 Oklahoma City Tornadic Supercell and Associated Tornadoes to Multimoment Microphysics. Part I: Storm- and Tornado-Scale Numerical Forecasts. *Mon. Wea. Rev.*, **143,** 2241-2265.

Dixon, M., Z.Li, H.Lean, N.Roberts, and S.Ballard, 2009: Impact of data assimilation on forecasting convection over the United Kingdom using a high-resolution version of the Met Office Unified Model. *Mon. Wea. Rev.*, **137,** 1562–1584.

Dowell, D. C., L. J. Wicker, and C. Snyder, 2011: Ensemble Kalman Filter Assimilation of Radar Observations of the 8 May 2003 Oklahoma City Supercell: Influences of Reflectivity Observations on Storm-Scale Analyses. *Mon. Wea. Rev.*, **139,** 272-294.

Dowell, D. C., F. Q. Zhang, L. J. Wicker, C. Snyder, and N. A. Crook, 2004: Wind and temperature retrievals in the 17 May 1981 Arcadia, Oklahoma, supercell: Ensemble Kalman filter experiments. *Mon. Wea. Rev.*, **132,** 1982-2005.

Du, N., M. Xue, K. Zhao, and J. Min, 2012: Impact of assimilating airborne Doppler radar velocity data using the ARPS 3DVAR on the analysis and prediction of Hurricane Ike (2008). *J. Geophys. Res. Atmos.*, **117**, D18113.

Etherton, B. J., and C. H. Bishop, 2004: Resilience of hybrid ensemble/3DVAR analysis schemes to model error and ensemble covariance error. *Mon. Wea. Rev.*, **132,** 1065-1080.

Evensen, G., 1994: Sequential Data Assimilation with a Nonlinear Quasi-Geostrophic Model Using Monte-Carlo Methods to Forecast Error Statistics. *J. Geophys. Res-Oceans.*, **99,** 10143-10162.

Gao, J., C. H. Fu, D. J. Stensrud, and J. S. Kain, 2016: OSSEs for an Ensemble 3DVAR Data Assimilation System with Radar Observations of Convective Storms. *J. Atmos. Sci.*, **73,** 2403-2426.

Gao, J., and D. J. Stensrud, 2012: Assimilation of Reflectivity Data in a Convective-Scale, Cycled 3DVAR Framework with Hydrometeor Classification. *J. Atmos. Sci.*, **69,** 1054-1065.

——, 2014: Some Observing System Simulation Experiments with a Hybrid 3DEnVAR System for Storm-Scale Radar Data Assimilation. *Mon. Wea. Rev.*, **142,** 3326-3346.

Gao, J., M. Xue, K. Brewster, and K. Droegemeier, 2004: Three-Dimensional Variational Data Analysis Method with Recursive Filter for Doppler Radars. *J. Atm. Ocean. Tech.*, **21,** 457-469.

Gao, J., M. Xue, and D. J. Stensrud, 2013: The Development of a Hybrid EnKF-3DVAR Algorithm for Storm-Scale Data Assimilation. Adv. Meteor., 2013, http://dx.doi.org/10.1155/2013/512656.

Gaspari, G., and S. E. Cohn, 1999: Construction of correlation functions in two and three dimensions. *Quart. J. Roy. Met. Soc.*, **125,** 723-757.

Ge, G., J. Gao, and M. Xue, 2012: Diagnostic Pressure Equation as a Weak Constraint in a Storm-Scale Three-Dimensional Variational Radar Data Assimilation System. *J. Atm. Ocean. Tech.*, **29,** 1075-1092.

——, 2013: Impacts of Assimilating Measurements of Different State Variables with a Simulated Supercell Storm and Three-Dimensional Variational Method. *Mon. Wea. Rev.*, **141,** 2759-2777.

Greybush, S. J., E. Kalnay, T. Miyoshi, K. Ide, and B. R. Hunt, 2011: Balance and Ensemble Kalman Filter Localization Techniques. *Mon. Wea. Rev.*, **139,** 511-522.

Grzych, M. L., B. D. Lee, and C. A. Finley, 2007: Thermodynamic analysis of supercell rear-flank downdrafts from project ANSWERS. *Mon. Wea. Rev.*, **135,** 240-246.

Gustafsson, N., and Coauthors, 2018: Survey of data assimilation methods for convective-scale numerical weather prediction at operational centres. *Quart. J. Roy. Met. Soc.*, **144,** 1218-1256.

Hamill, T. M., and C. Snyder, 2000: A hybrid ensemble Kalman filter-3D variational analysis scheme. *Mon. Wea. Rev.*, **128,** 2905-2919.

Hirth, B. D., J. L. Schroeder, and C. C. Weiss, 2008: Surface analysis of the rear-flank downdraft outflow in two tornadic supercells. *Mon. Wea. Rev.*, **136,** 2344-2363.

Houtekamer, P. L., H. L. Mitchell, G. Pellerin, M. Buehner, M. Charron, L. Spacek, and M. Hansen, 2005: Atmospheric data assimilation with an ensemble Kalman filter: Results with real observations. *Mon. Wea. Rev.*, **133**, 604-620.

Hu, M., M. Xue, and K. Brewster, 2006: 3DVAR and cloud analysis with WSR-88D level-II data for the prediction of the Fort Worth, Texas, Tornadic thunderstorms. Part I: Cloud analysis and its impact. *Mon. Wea. Rev.*, **134,** 675-698.

Jung, Y., M. Xue, and M. Tong, 2012a: Ensemble Kalman Filter Analyses of the 29-30 May 2004 Oklahoma Tornadic Thunderstorm Using One- and Two-Moment Bulk Microphysics Schemes, with Verification against Polarimetric Radar Data. *Mon. Wea. Rev.*, **140,** 1457-1475.

Jung, Y., M. Xue, Y. Wang, Y. Pan, and K. Zhu, 2012b: Tests of a cycled EnKF data assimilation and forecasts for the 10 May 2010 tornado outbreak in the central US domain. *25th Conf. on Severe and Local Storms***,** Nashville, TN, Amer. Meteor. Soc., 8A.4, https://ams.confex.com/ams/26SLS/webprogram/Paper211285.html.

Jung, Y., M. Xue, Y. Wang, S. Wang, F. Kong, Y. Pan, and K. Zhu, 2013: Multi-scale ensemble Kalman filter data assimilation and forecasts in central United States. *6th WMO Symposium on Symposium on DA*. http://das6.umd.edu/program/Posters/uploads/Bp09-Jung_Youngsun.pdf.

Jung, Y., M. Xue, and G. Zhang, 2010: Simultaneous Estimation of Microphysical Parameters and the Atmospheric State Using Simulated Polarimetric Radar Data and an Ensemble Kalman Filter in the Presence of an Observation Operator Error. *Mon. Wea. Rev.*, **138,** 539-562.

Jung, Y., M. Xue, G. Zhang, and J. M. Straka, 2008: Assimilation of simulated polarimetric radar data for a convective storm using the ensemble Kalman filter. Part II: Impact of polarimetric data on storm analysis. *Mon. Wea. Rev.*, **136,** 2246-2260.

Kain, J. S., and Coauthors, 2008: Some Practical Considerations Regarding Horizontal Resolution in the First Generation of Operational Convection-Allowing NWP. *Wea. Forecasting*, **23,** 931-952.

Kain, J. S., and Coauthors, 2010: Assessing Advances in the Assimilation of Radar Data and Other Mesoscale Observations within a Collaborative Forecasting-Research Environment. *Wea. Forecasting*, **25,** 1510-1521.

Kepert, J. D., 2009: Covariance localisation and balance in an Ensemble Kalman Filter. *Quart. J. Roy. Met. Soc.*, **135,** 1157-1176.

Kong, R., M. Xue, and C. Liu, 2018: Development of a Hybrid En3DVar Data Assimilation System and Comparisons with 3DVar and EnKF for Radar Data Assimilation with Observing System Simulation Experiments. *Mon. Wea. Rev.*, **146,** 175-198.

Li, Y., X. Wang, and M. Xue, 2012: Assimilation of Radar Radial Velocity Data with the WRF Hybrid Ensemble-3DVAR System for the Prediction of Hurricane Ike (2008). *Mon. Wea. Rev.*, **140,** 3507-3524.

Lin, Y., R. D. Farley, and H. D. Orville, 1983: Bulk Parameterization of the Snow Field in a Cloud Model. *J. Clim. Appl. Meteorol.*, **22,** 1065-1092.

Liu, C., and M. Xue, 2016: Relationships among Four-Dimensional Hybrid Ensemble-Variational Data Assimilation Algorithms with Full and Approximate Ensemble Covariance Localization. *Mon. Wea. Rev.*, **144,** 591-606.

Liu, C., M. Xue, and R. Kong, 2019: Direct Assimilation of Radar Reflectivity Data Using 3DVAR: Treatment of Hydrometeor Background Errors and OSSE Tests. *Mon. Wea. Rev.*, **147,** 17-29.

——, 2020: Direct variational assimilation of radar reflectivity and radial velocity data: Issues with nonlinear reflectivity operator and solutions. *Mon. Wea. Rev.*, DOI 10.1175/MWR-D-1119-0149.1171.

Liu, H., and M. Xue, 2008: Prediction of convective initiation and storm evolution on 12 June 2002 during IHOP_2002. Part I: Control simulation and sensitivity experiments. *Mon. Wea. Rev.*, **136,** 2261-2282.

Lorenc, A. C., 2003: The potential of the ensemble Kalman filter for NWP - a comparison with 4D-Var. *Quart. J. Roy. Met. Soc.*, **129,** 3183-3203.

Manobianco, J., S.Koch, V. M.Karyampudi, and A. J.Negri, 1994: The impact of assimilating satellite-derived precipitation rates on numerical simulations of the ERICA IOP 4 cyclone. *Mon. Wea. Rev.,*, **122,** 341–365.

Markowski, P. M., and Y. P. Richardson, 2014: The Influence of Environmental Low-Level Shear and Cold Pools on Tornadogenesis: Insights from Idealized Simulations. *J. Atmos. Sci.*, **71,** 243-275.

Markowski, P. M., J. M. Straka, and R. E. N., 2002: Direct surface thermodynamic observations within the rear-flank downdrafts of nontornadic and tornadic supercells. *Mon. Wea. Rev.*, **130,** 1692-1721.

Noilhan, J., and S. Planton, 1989: A Simple Parameterization of Land Surface Processes for Meteorological Models. *Mon. Wea. Rev.*, **117,** 536-549.

Pan, Y., and Coauthors, 2014: A GSI-Based Coupled EnSRF-En3DVar Hybrid Data Assimilation System for the Operational Rapid Refresh Model: Tests at a Reduced Resolution. *Mon. Wea. Rev.*, **142,** 3756-3780.

Simonin, D., C.Pierce, N.Roberts, S. P.Ballard, and Z.Li, 2017: Performance of Met Office hourly cycling NWP-based nowcasting for precipitation forecasts. *Quart. J. Roy. Meteor. Soc.*, **143,** 2862–2873.

Snook, N., M. Xue, and Y. Jung, 2011: Analysis of a Tornadic Mesoscale Convective Vortex Based on Ensemble Kalman Filter Assimilation of CASA X-Band and WSR-88D Radar Data. *Mon. Wea. Rev.*, **139,** 3446-3468.

——, 2012: Ensemble Probabilistic Forecasts of a Tornadic Mesoscale Convective System from Ensemble Kalman Filter Analyses Using WSR-88D and CASA Radar Data. *Mon. Wea. Rev.*, **140,** 2126-2146.

Snook, N., M. Xue, and Y. Jung, 2019: Tornado-resolving ensemble and probabilistic predictions of the 20 May 2013 Newcastle-Moore EF5 tornado. *Mon. Wea. Rev.*, **147**, 1215-1235.

Snyder, C., and F. Q. Zhang, 2003: Assimilation of simulated Doppler radar observations with an ensemble Kalman filter. *Mon. Wea. Rev.*, **131,** 1663-1677.

Stensrud, D. J., and Coauthors, 2013: Progress and challenges with Warn-on-Forecast. *Atmos. Res.*, **123,** 2-16.

Stratman, D. R., N. Yussouf, Y. Jung, T. A. Supinie, M. Xue, P. S. Skinner, and B. J. Putnam, 2020: Optimal temporal frequency of phased-array radar observations for storm-scale data assimilation. *Wea. Forecasting*, **35**, 193-214.

Sugimoto, S., N. A. Crook, J. Sun, Q. N. Xiao, and D. M. Barker, 2009: An Examination of WRF 3DVAR Radar Data Assimilation on Its Capability in Retrieving Unobserved Variables and Forecasting Precipitation through Observing System Simulation Experiments. *Mon. Wea. Rev.*, **137,** 4011-4029.

Sun, J., and A. Crook, 1994: Wind and Thermodynamic Retrieval from Single-Doppler Measurements of a Gust Front Observed during Phoenix-Ii. *Mon. Wea. Rev.*, **122,** 1075-1091.

Sun, J., and N. A. Crook, 1997: Dynamical and microphysical retrieval from Doppler radar observations using a cloud model and its adjoint .1. Model development and simulated data experiments. *J. Atmos. Sci.*, **54,** 1642-1661.

——, 1998: Dynamical and microphysical retrieval from Doppler radar observations using a cloud model and its adjoint. Part II: Retrieval experiments of an observed Florida convective storm. *J. Atmos. Sci.*, **55,** 835-852.

Sun, J., and Coauthors, 2014: Use of NWP for nowcasting convective precipitation: Recent progress and challenges. *Bull. Amer. Meteor. Soc.*, **95,** 409-426.

Sun, W., and C. Chang, 1986: Diffusion-Model for a Convective Layer .1. Numerical-Simulation of Convective Boundary-Layer. *J. Clim. Appl. Meteorol.*, **25,** 1445-1453.

Tong, M., and M. Xue, 2005: Ensemble Kalman filter assimilation of Doppler radar data with a compressible nonhydrostatic model: OSS experiments. *Mon. Wea. Rev.*, **133,** 1789-1807.

——, 2008: Simultaneous estimation of microphysical parameters and atmospheric state with simulated radar data and ensemble square root Kalman filter. Part I: Sensitivity analysis and parameter identifiability. *Mon. Wea. Rev.*, **136,** 1630-1648.

Wang, H., J. Sun, S. Fan, and X. Huang, 2013: Indirect Assimilation of Radar Reflectivity with WRF 3D-Var and Its Impact on Prediction of Four Summertime Convective Events. *J. Appl. Meteorol. Clim.*, **52,** 889-902.

Wang, H., J. Sun, Y.-R. Guo, and X.-Y. Huang, 2011: Radar Reflectivity Assimilation with the Updated WRFDA-4DVAR System**,** 15th Conference on IOAS-AOLS, Seattle, WA, *Amer. Meteor. Soc*., J17.14.

Wang, W., and T. T.Warner, 1988: Use of four-dimensional data assimilation by Newtonian relaxation and latent-heat forcing to improve a mesoscale-model precipitation forecast: A case study. *Mon. Wea. Rev.*, **116,** 2593–2613.

Wang, X., T. A. Hamill, J. S. Whitaker, and C. H. Bishop, 2007: A comparison of hybrid ensemble transform Kalman filter-optimum interpolation and ensemble square root filter analysis schemes. *Mon. Wea. Rev.*, **135,** 1055-1076.

Wang, Y., and X. Wang, 2017: Direct Assimilation of Radar Reflectivity without Tangent Linear and Adjoint of the Nonlinear Observation Operator in the GSI-Based EnVar System: Methodology and Experiment with the 8 May 2003 Oklahoma City Tornadic Supercell. *Mon. Wea. Rev, **145**, 1447-1471.*

Whitaker, J. S., and T. M. Hamill, 2002: Ensemble data assimilation without perturbed observations. *Mon. Wea. Rev.*, **130,** 1913-1924.

——, 2012: Evaluating Methods to Account for System Errors in Ensemble Data Assimilation. *Mon. Wea. Rev.*, **140,** 3078-3089.

WSEC, 2006: A recommendation for an enhanced Fujita scale (EF-scale). . *Texas Tech University Wind Science and Engineering Center Rep.***,** 95pp. [Available online at www.depts.ttu.edu/weweb/pubs/fscale/efscale.pdf.].

Wu, W.-S., R. J. Purser, and D. F. Parrish, 2002: Three-dimensional variational analysis with spatially inhomogeneous covariances. *Mon. Wea. Rev.*, **130,** 2905-2916.

Xiao, Q., Y. H. Kuo, J. Sun, W. C. Lee, D. M. Barker, and E. Lim, 2007: An approach of radar reflectivity data assimilation and its assessment with the inland QPF of Typhoon Rusa (2002) at landfall. *J. Appl. Meteorol. Clim.*, **46,** 14-22.

Xiao, Q., Y. Kuo, J. Sun, W. C. Lee, E. Lim, Y. Guo, and D. M. Barker, 2005: Assimilation of Doppler radar observations with a regional 3DVAR system: Impact of Doppler velocities on forecasts of a heavy rainfall case. *J. Appl. Meteor.*, **44,** 768-788.

Xue, M., K. K. Droegemeier, and V. Wong, 2000: The Advanced Regional Prediction System (ARPS) - A multi-scale nonhydrostatic atmospheric simulation and prediction model. Part I: Model dynamics and verification. *Meteor. Atmos. Physics*, **75,** 161-193.

Xue, M., and Coauthors, 2001: The Advanced Regional Prediction System (ARPS) - A multi-scale nonhydrostatic atmospheric simulation and prediction tool. part II: Model physics and applications. *Meteor. Atmos. Physics*, **76,** 143-165.

Xue, M., M. Hu, and A. D. Schenkman, 2014: Numerical Prediction of the 8 May 2003 Oklahoma City Tornadic Supercell and Embedded Tornado Using ARPS with the Assimilation of WSR-88D Data. *Wea. Forecasting*, **29,** 39-62.

Xue, M., F. Kong, K. W. Thomas, J. Gao, Y. Wang, K. Brewster, and K. K. Droegemeier, 2013: Prediction of Convective Storms at Convection-Resolving 1km Resolution over Continental United States with Radar Data Assimilation: An Example Case of 26 May 2008 and Precipitation Forecasts from Spring 2009. *Adv. Meteorol.*

Xue, M., and W. J. Martin, 2006: A high-resolution modeling study of the 24 May 2002 dryline case during IHOP. Part I: Numerical simulation and general evolution of the dryline and convection. *Mon. Wea. Rev.*, **134,** 149-171.

Xue, M., M. Tong, and K. K. Droegemeier, 2006: An OSSE framework based on the ensemble square root Kalman filter for evaluating the impact of data from radar networks on thunderstorm analysis and forecasting. *J. Atm. Ocean. Tech.*, **23,** 46-66.

Xue, M., M. Tong, and G. Zhang, 2009: Simultaneous state estimation and attenuation correction for thunderstorms with radar data using an Ensemble Kalman Filter: Tests with simulated data. *Quart. J. Roy. Met. Soc.*, **135,** 1409-1423.

Xue, M., D. Wang, J. Gao, K. Brewster, and K. K. Droegemeier, 2003: The Advanced Regional Prediction System (ARPS), storm-scale numerical weather prediction and data assimilation. *Meteor. Atmos. Physics*, **82,** 139-170.

Yussouf, N., and D. J. Stensrud, 2010: Impact of Phased-Array Radar Observations over a Short Assimilation Period: Observing System Simulation Experiments Using an Ensemble Kalman Filter. *Mon. Wea. Rev.*, **138,** 517-538.

Zhang, F., C. Snyder, and J. Sun, 2004: Impacts of initial estimate and observation availability on convective-scale data assimilation with an ensemble Kalman filter. *Mon. Wea. Rev.*, **132,** 1238-1253.

Zhang, M., F. Zhang, X. Huang, and X. Zhang, 2011: Intercomparison of an Ensemble Kalman Filter with Three- and Four-Dimensional Variational Data Assimilation Methods in a Limited-Area Model over the Month of June 2003. *Mon. Wea. Rev.*, **139,** 566-572.

Zhang, M., M. Zupanski, M. J. Kim, and J. A. Knaff, 2013: Assimilating AMSU-A Radiances in the TC Core Area with NOAA Operational HWRF (2011) and a Hybrid Data Assimilation System: Danielle (2010). *Mon. Wea. Rev.*, **141,** 3889-3907.

Zhao, K., and M. Xue, 2009: Assimilation of coastal Doppler radar data with the ARPS 3DVAR and cloud analysis for the prediction of Hurricane Ike (2008). *Geophys. Res. Lett.*, **36**.

Table 1 Descriptions of the assimilating experiments. Suffix "_CVq" indicates using mixing ratios q_x ($x = r, s, h$ are mixing ratios of rain, snow and hail) as the control variables, while "CVlogq" indicates using $log_{10}^{q_x}$ as the control variables.

Experiment name.	Use of background error covariance	Analysis updating
CTRL (no DA)	N.A.	N.A.
EnKF	100% ensemble covariance	Updates ensemble mean background forecast and ensemble perturbations using EnSRF algorithm.
DfEnKF	100% ensemble covariance	Updates a single deterministic background forecast using EnSRF ensemble mean updating algorithm.
HEn3DVar0%B_CVq/CVlogq (or PEn3DVar_CVq/CVlogq)	0% static & 100% ensemble covariance	Updates a single deterministic background forecast using En3DVar algorithm.
HEn3DVar5%B_CVq/CVlogq	5% static & 95% ensemble covariance	
HEn3DVar25%B_CVq/CVlogq	25% static & 75% ensemble covariance	
HEn3DVar50%B_CVq/CVlogq	50% static & 50% ensemble covariance	
HEn3DVar75%B_CVq/CVlogq	75% static & 25% ensemble covariance	
HEn3DVar100%B_CVq/CVlogq (or 3DVar_CVq/CVlogq)	100% static & 0% ensemble covariance	

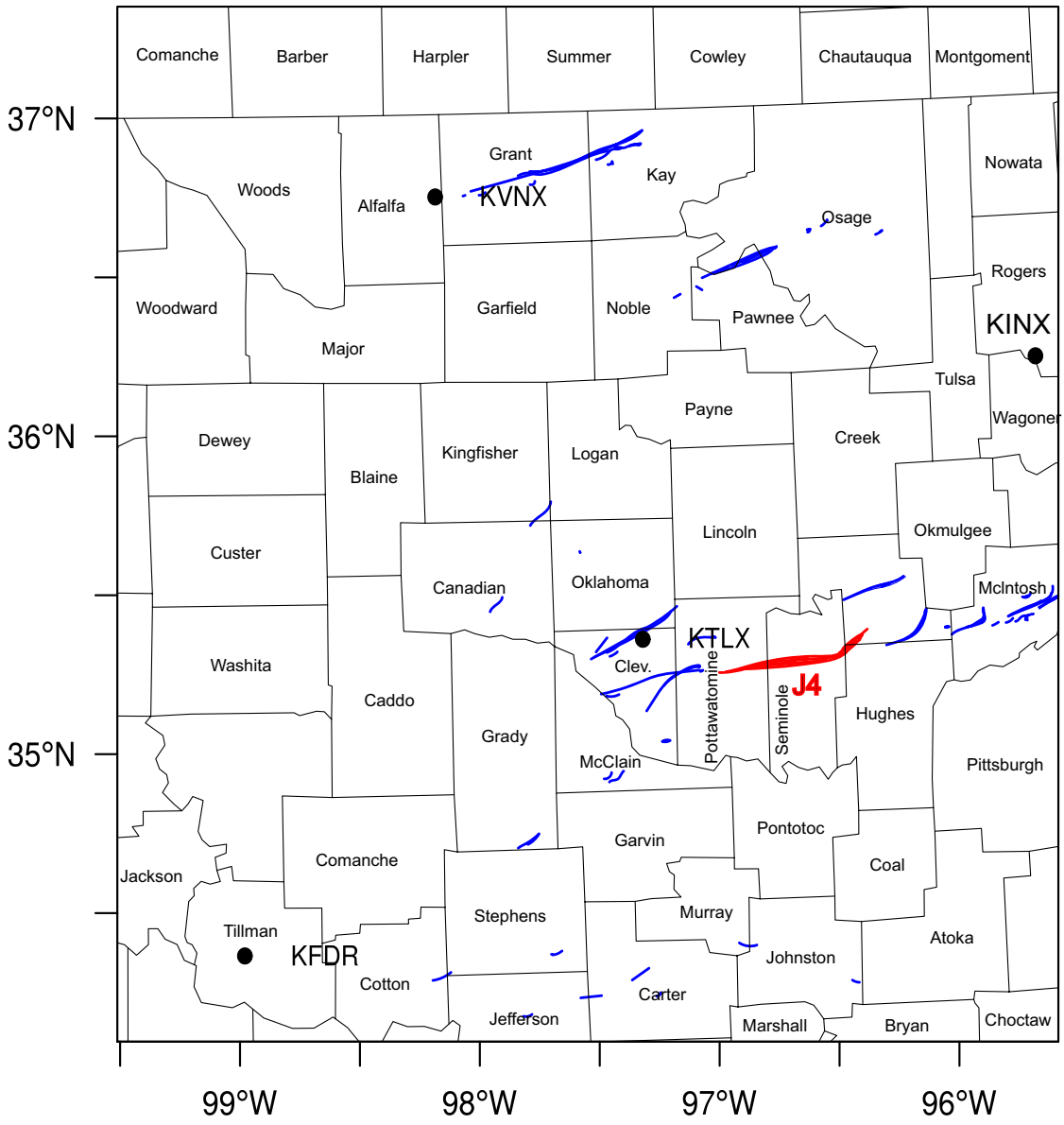

Fig. 1 The model and DA domain and locations of four S-band WSR-88D radars (KTLX, KVNX, KFDR, and KINX as marked by the black dots) whose data are assimilated, overlaid with the damage paths of tornadoes (blue and red trajectories) that occurred in Oklahoma on May 10, 2010. The red trajectory indicates the damage path of the EF3 storm simulated in this study.

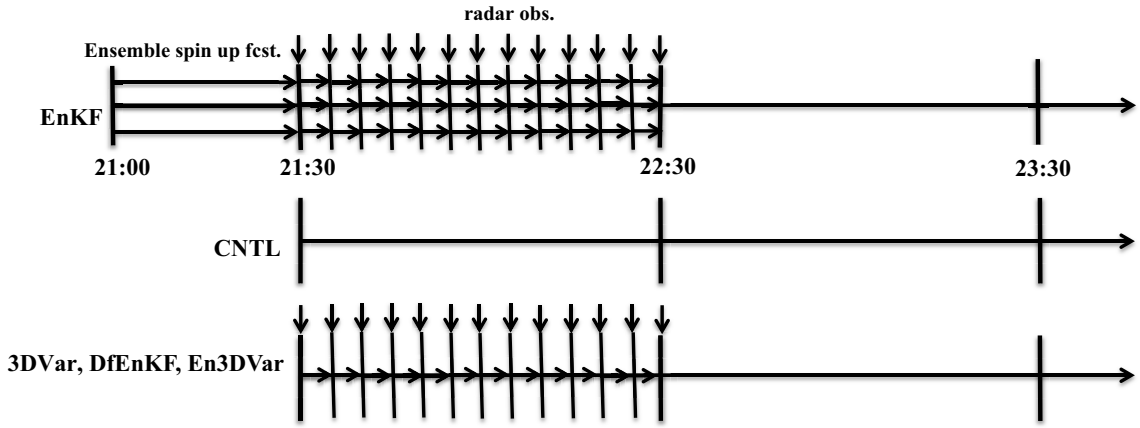

Fig. 2 The flow diagrams of DA experiments.

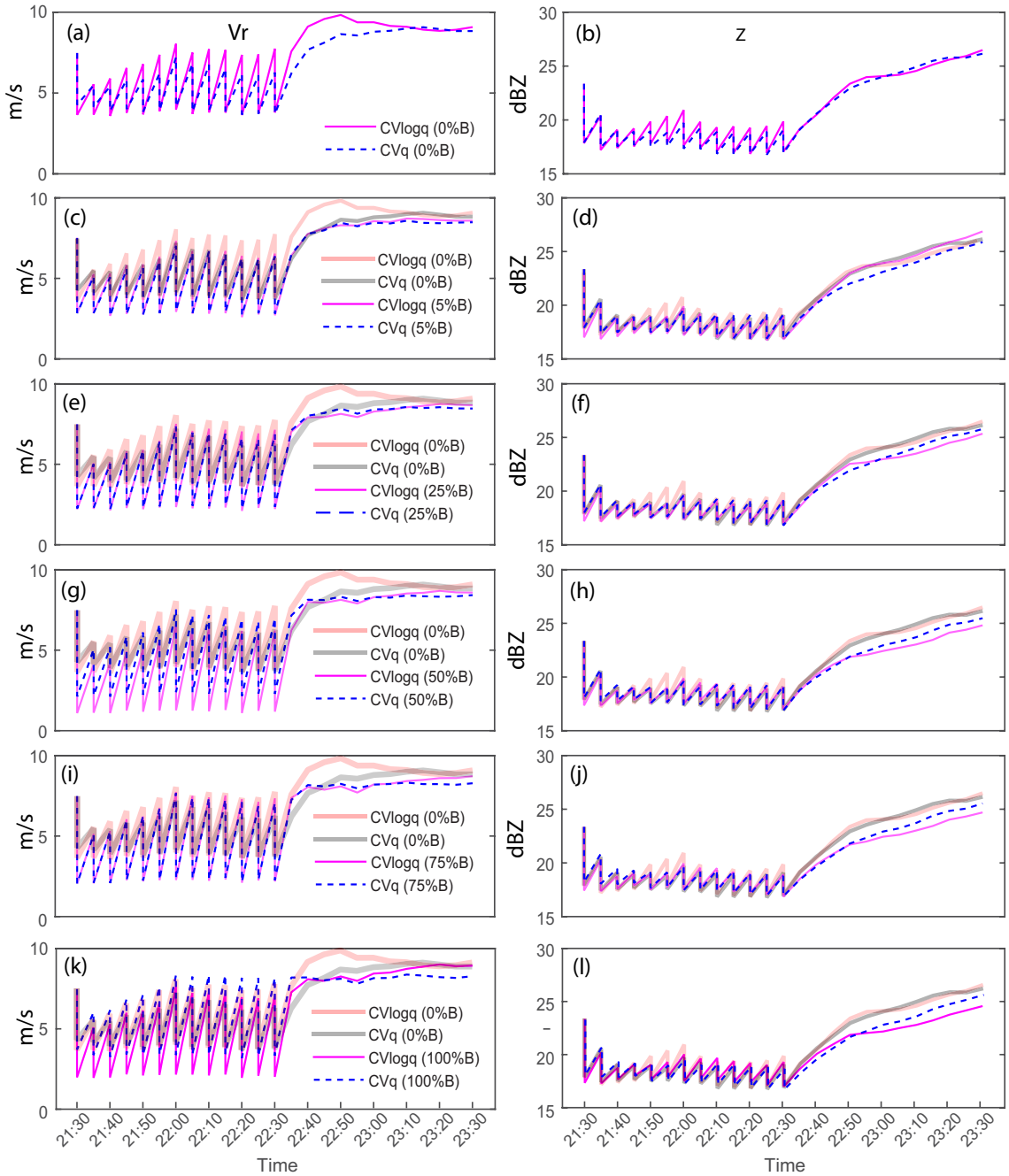

Fig. 3 Comparisons of the RMSIs of (a, c, e, g, i) radial velocity (m s^{-1}) and (b, d, f, h, j) reflectivity (dBZ) analyses and forecasts from hybrid En3DVar with (a, b) 0%, (c, d) 5%, (e, f), 25%, (g, h) 50%, (i, j) 75%, and (k, l) 100% weight of static **B** for CVq and CVlogq, respectively. The RMSIs of hybrid En3DVar with 0% **B** are also overlaid in Figs (c) - (l) as references.

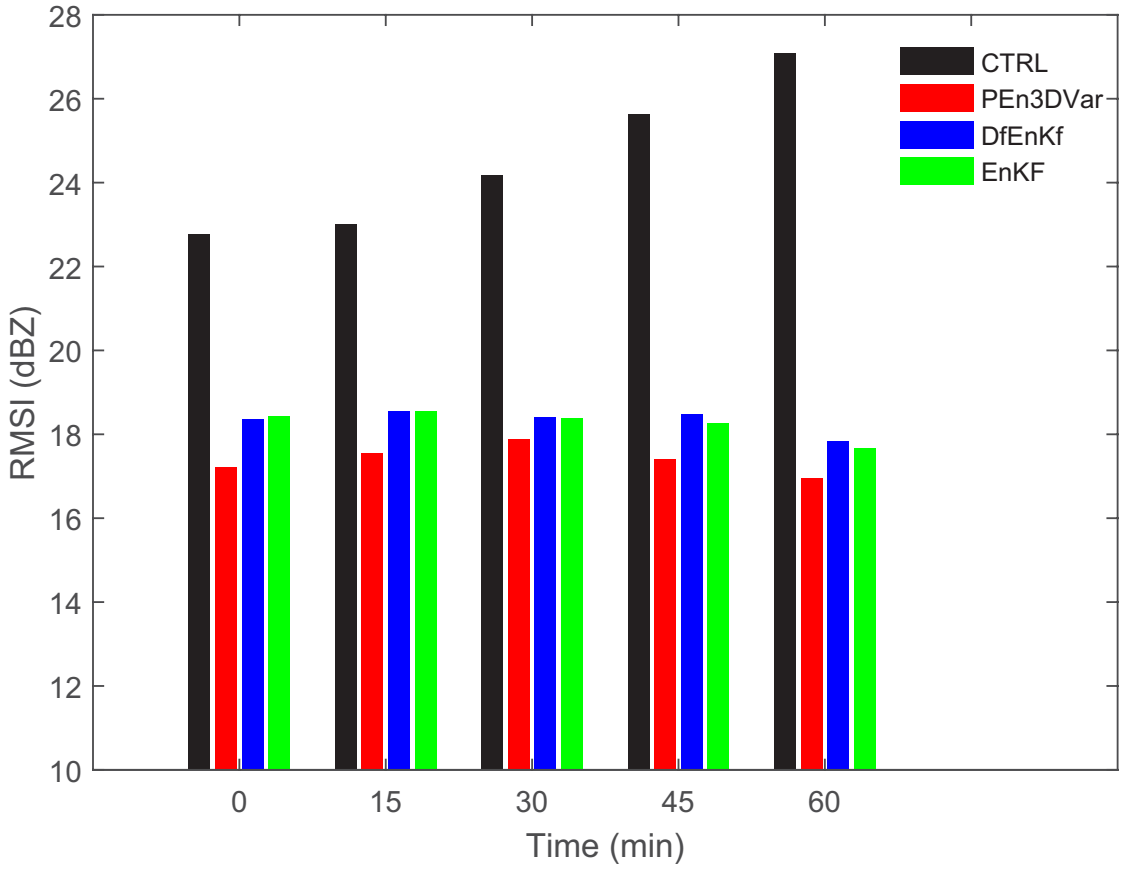

Fig. 4 Comparisons of the RMSIs of the analyzed reflectivity from CTRL, PEn3DVar, EnKF, and DfEnKF.

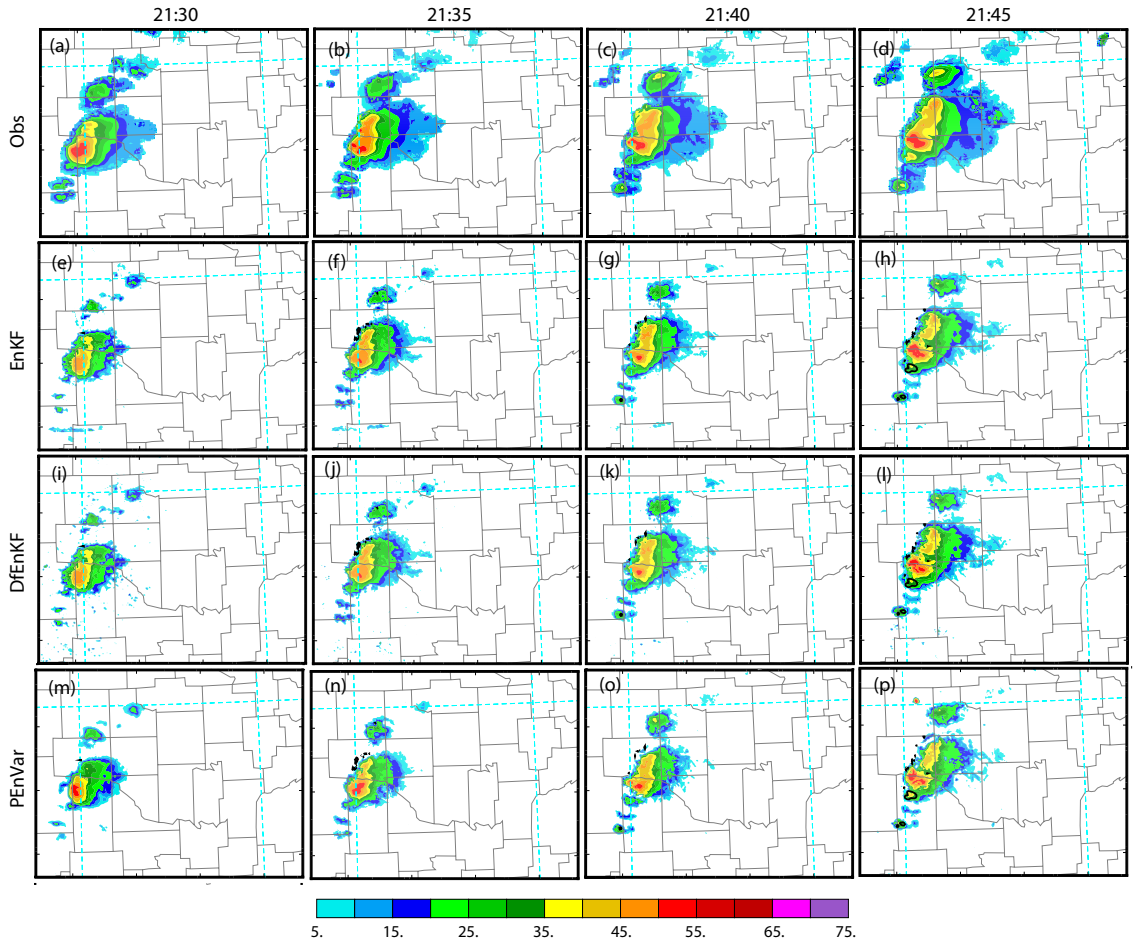

Fig. 5 Reflectivity observations (a - d) and analyses at 8 km AGL from (e – h) EnKF, (i – l) DfEnKF, and (m – p) PEn3DVar for the beginning four DA cycles, valid at (a, e, i, m) 2130 UTC, (b, f, j, n) 2135 UTC, (c, g, k, o) 2140 UTC, and (d, h, l, p) 21:45 UTC, respectively.

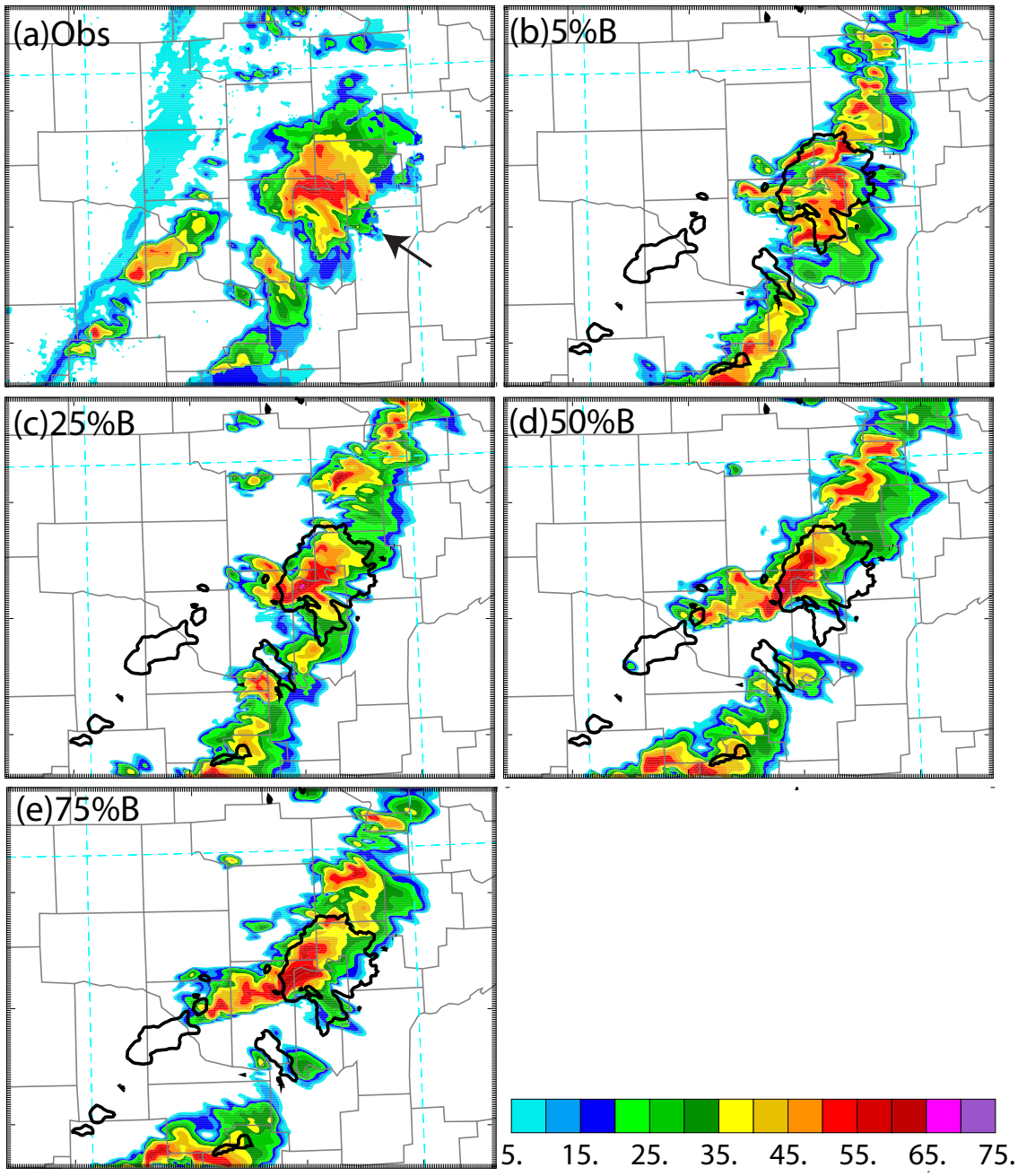

Fig. 6 (a) reflectivity observations and 45-minute reflectivity forecasts at 1 km AGL from hybrid En3DVar with (b) 5%, (c) 25%, (d) 50%, and (e) 75% weight of the static background error covariance **B**, overlaid with observed reflectivity contour that is equal to 35 dBZ. The Seminole storm is pointed to by an arrow in (a).

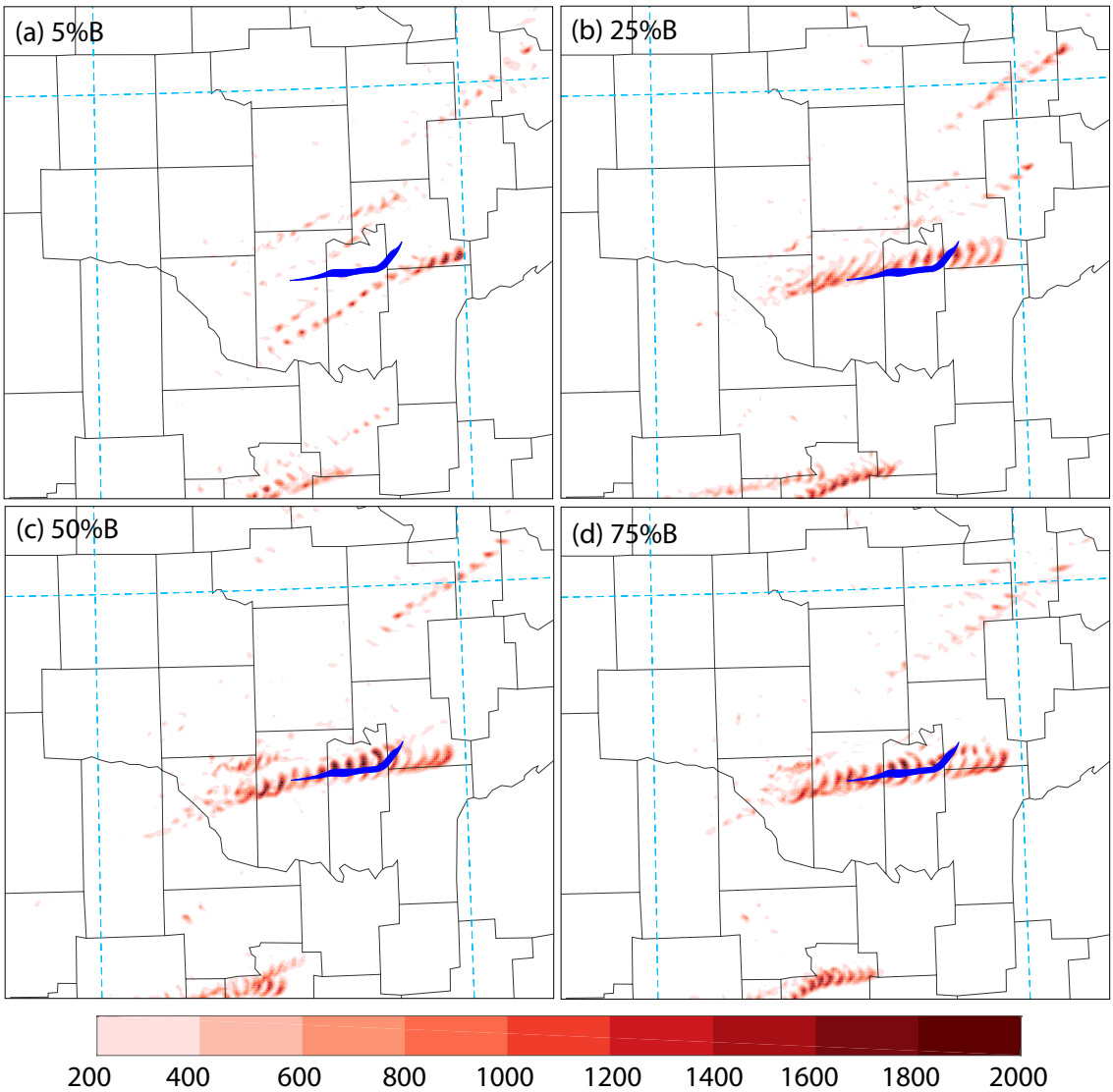

Fig. 7 Swaths of 0 - 1.5 h forecasts of 2 - 5 km updraft helicity (UH) greater than 200 $m^2 s^{-2}$ (shaded contours) from hybrid En3DVar with (a) 5% , (b) 25% , (c) 50%, and (d) 75% weight of the static **B**, overlaid with the Seminole tornado (J4) damage path (blue contour). The plotted UH swaths are composited from model output of UH at 5 min intervals.

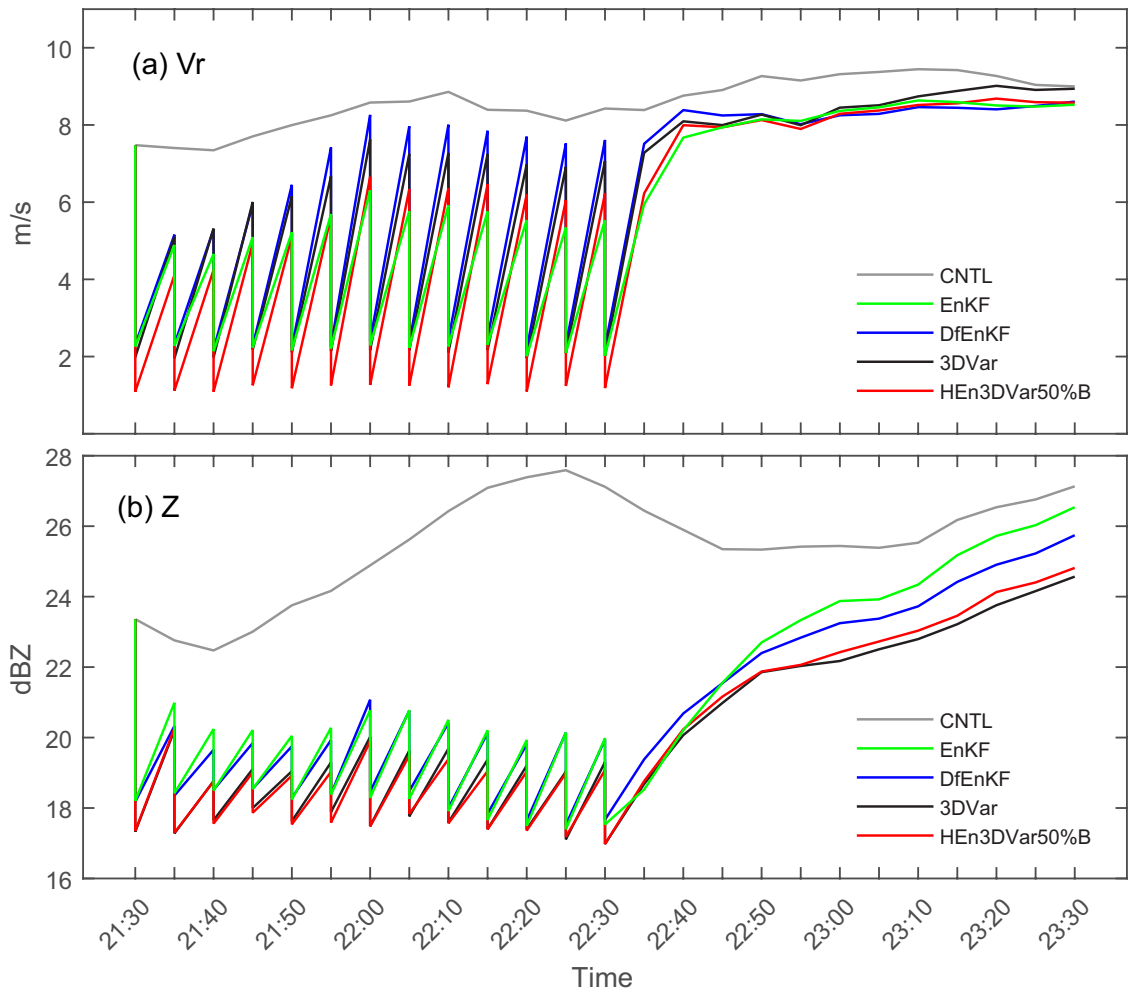

Fig. 8 Comparisons of the RMSIs of (a) radial velocity and (b) reflectivity analyses and forecasts from CNTL, EnKF, DfEnKF, 3DVar, and hybrid En3DVar algorithm with 50% static **B**, as indicated by legends in the figure.

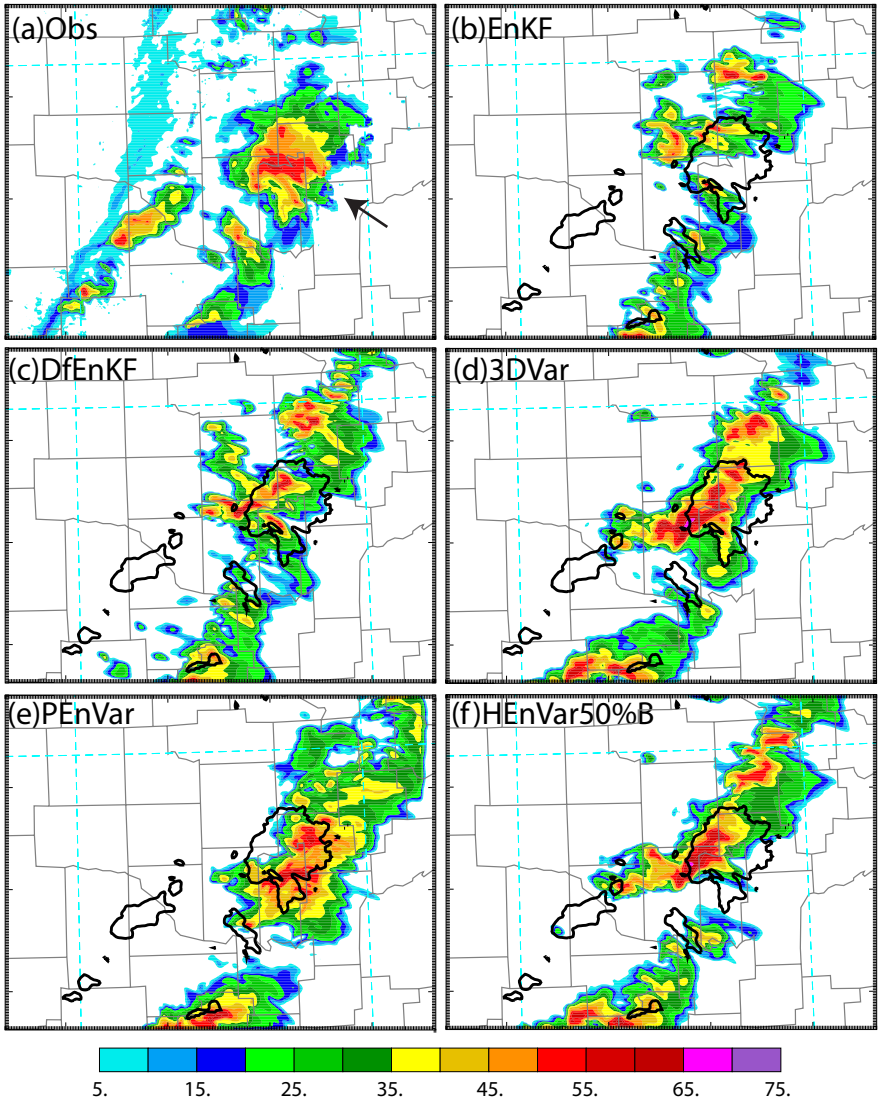

Fig. 9 (a) reflectivity observation and 45-min reflectivity forecasts at 1 km AGL from (b) EnKF, (c) DfEnKF, (d) 3DVar, (e) pure En3DVar, and (f) hybrid En3DVar with 50% static B, overlaid with observed 35 dBZ reflectivity contours. The Seminole storm is pointed to by an arrow in (a).

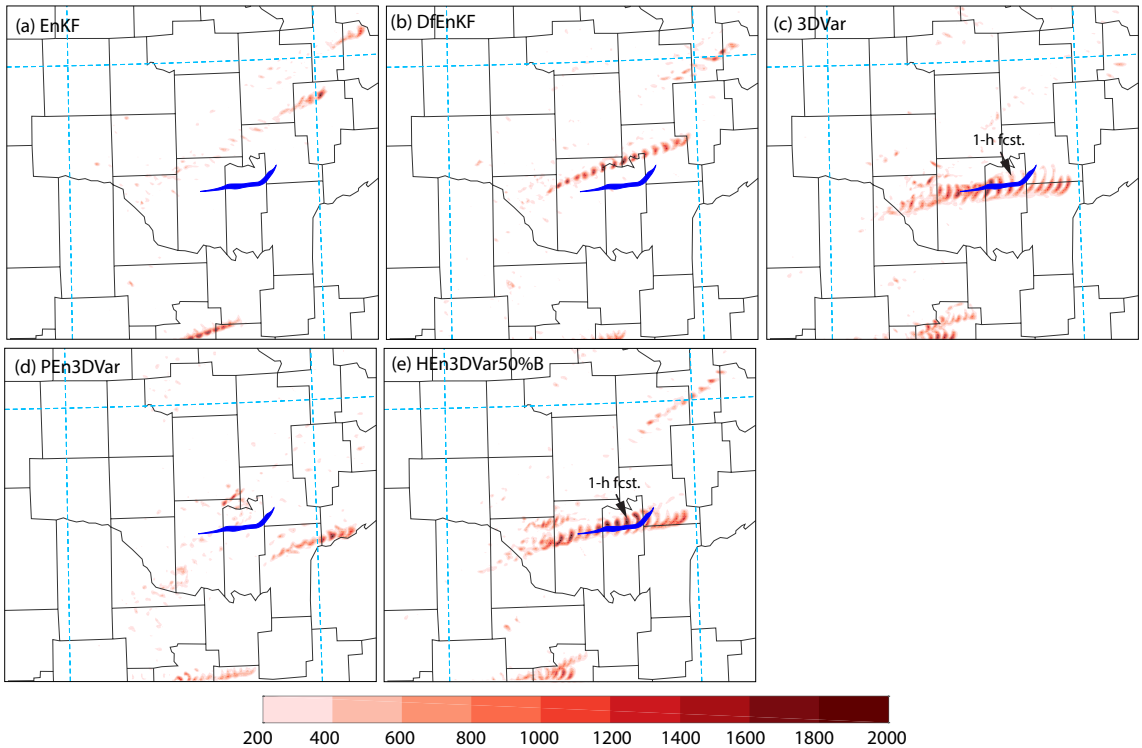

Fig. 10 Swaths of 0 - 1.5 h forecasts of 2 - 5 km updraft helicity greater than 200 m^2s^{-2} (shaded contours) from (a) EnKF, (b) DfEnKF, (c) 3DVar, (d) pure En3DVar, and (e) hybrid En3DVar with 50% weight of the static **B**, overlaid with the EF3 tornado Seminole damage path (blue contour).

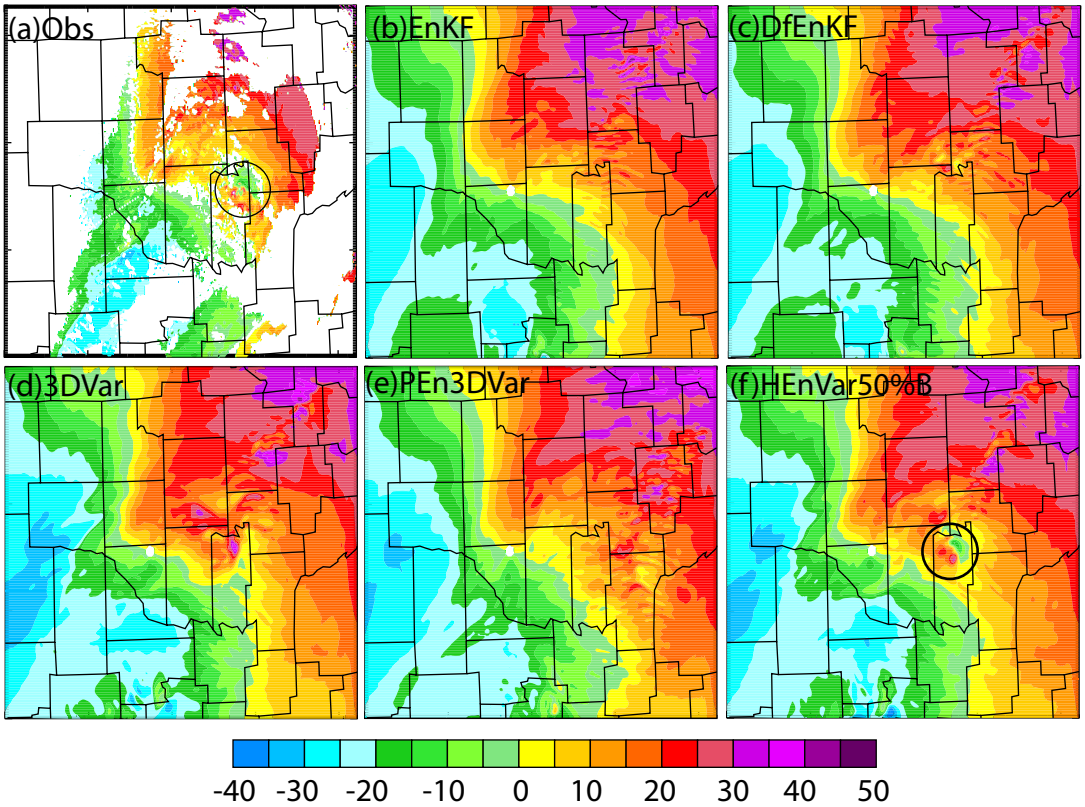

Fig. 11 (a) radial velocity observation and 1-h radial velocity forecasts at the lowest elevation angle of KTLX (0.5°) from (b) EnKF, (c) DfEnKF, (d) 3DVar, (e) pure En3DVar, and (f) hybrid En3DVar with 50% weight of static **B** (or HEn3DVar50%B) with the velocity couplet circled in black.

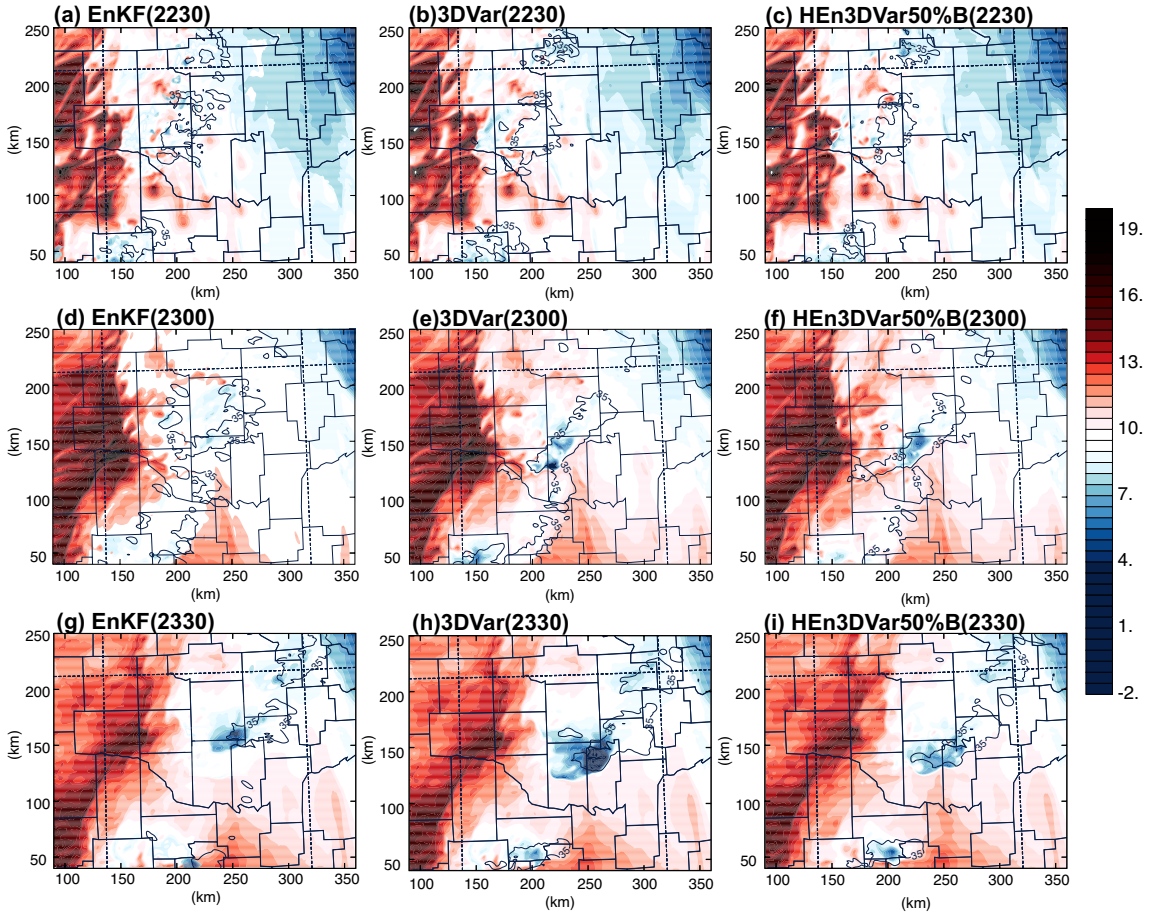

Fig. 12 Perturbations of the surface potential temperature (K) for (a, b, c) the analyses after 60-min DA (valid at 2230 UTC), (d, e, f) 30-min (valid at 2300 UTC), and (g, h, i) 60-min forecasts after DA (valid at 2330 UTC) from (a, d, g) DfEnKF, (b, e, h) 3DVar, and (c, f, i) HEn3DVar50%B, respectively.

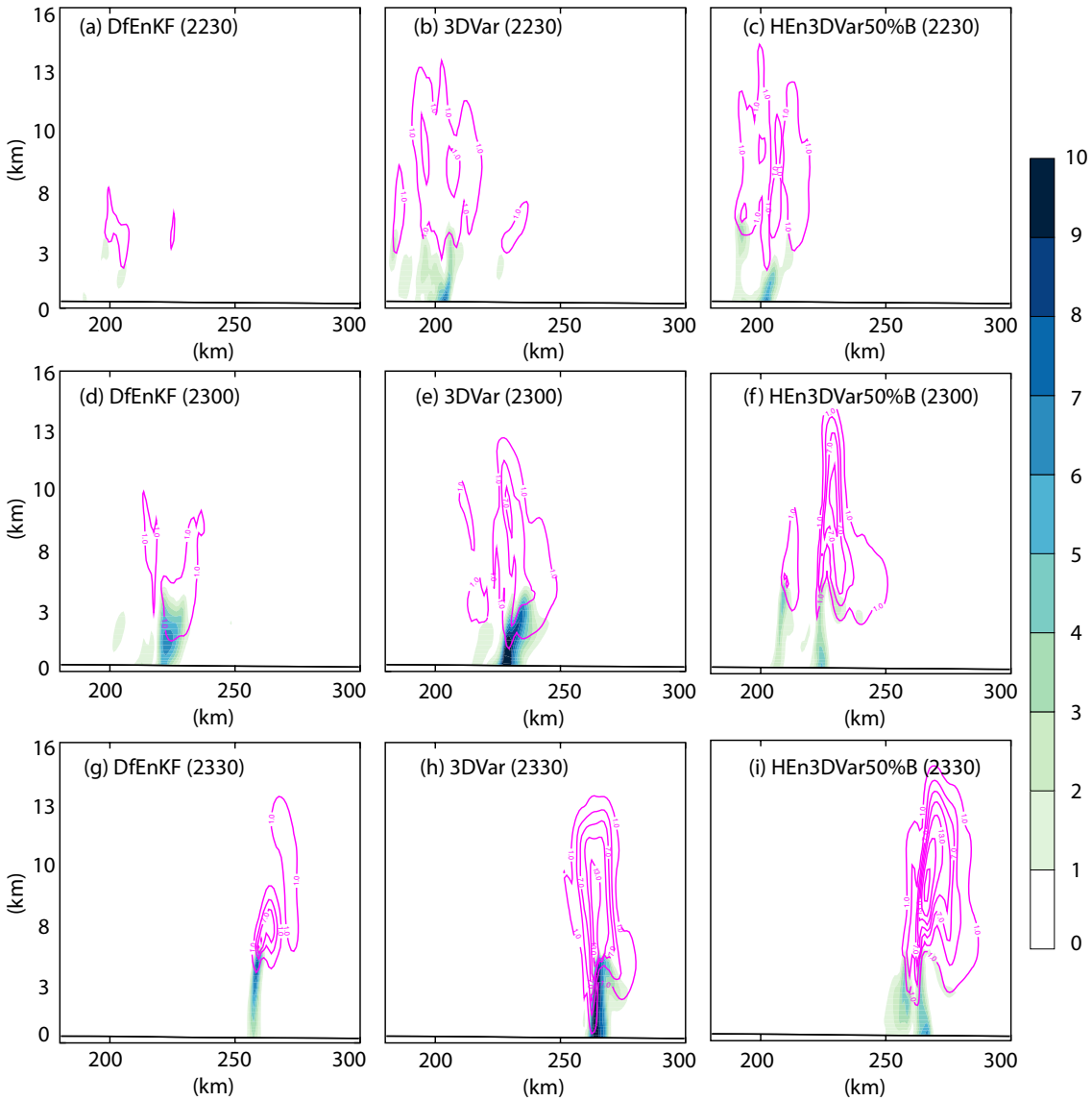

Fig. 13 Vertical cross-sections (through the maximum vertical velocities) of the hydrometeor mixing ratios of the rainwater (g kg^{-1}, shaded contours) and hail (g kg^{-1}, magenta contours, from 1 to 20 with interval of 3 g kg^{-1}) for (a, b, c) the analyses after 60-min DA (valid at 2230 UTC) and (d, e, f) the 30-min (valid at 2300 UTC), and (g, h, i) 60-min forecasts after DA (valid at 2330 UTC) from (a, d, g) DfEnKF, (b, e, h) 3DVar, and (c, f, i) HEn3DVar50%B, respectively.

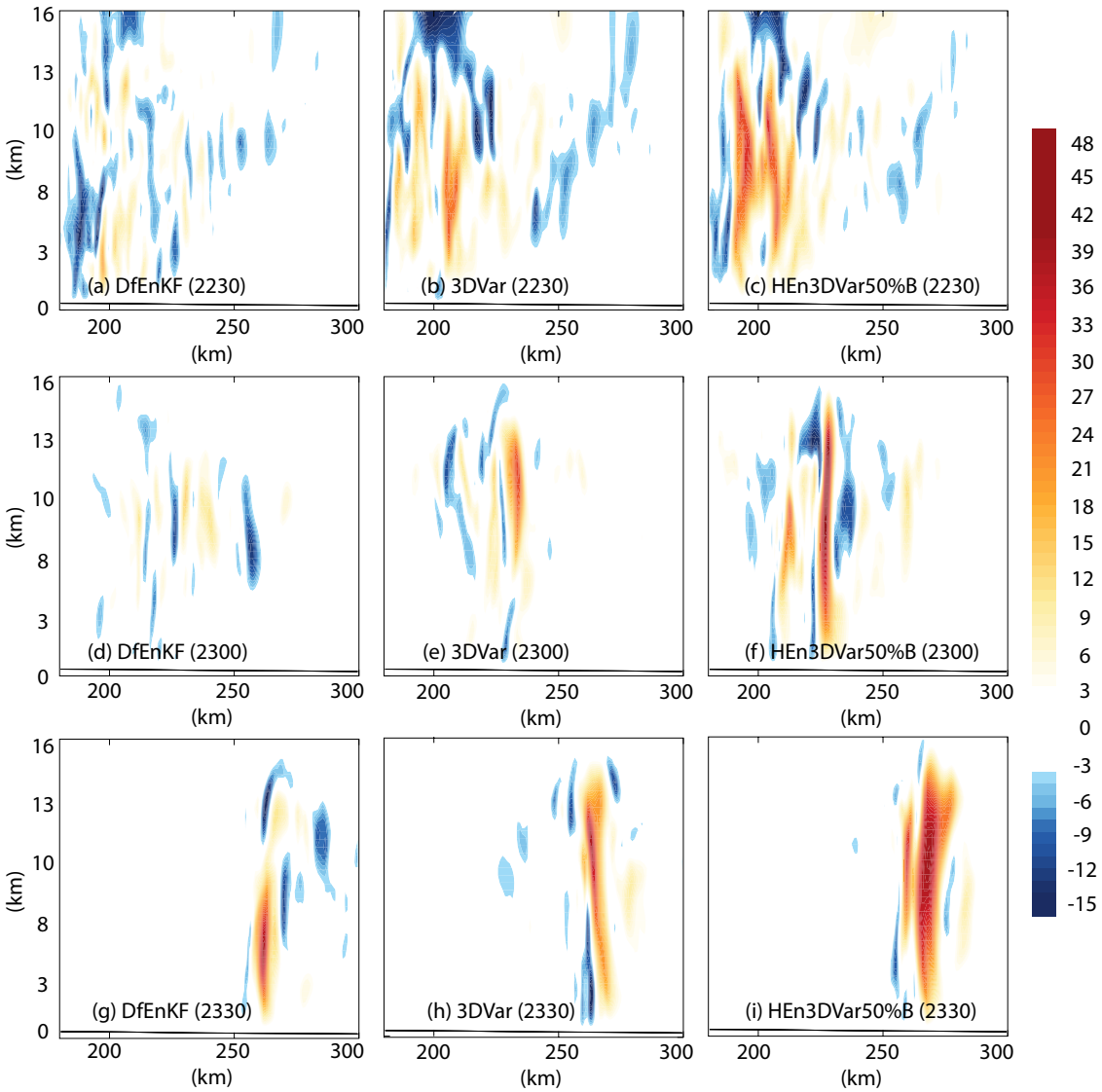

Fig. 14 Vertical cross-sections of the vertical velocity field (m s^{-1}, through their maximum values) for (a, b, c) the analyses after 60-min DA (valid at 2230 UTC) and (d, e, f) the 30-min (valid at 2300 UTC), and (g, h, i) 60-min forecasts after DA (valid at 2330 UTC) from (a, d, g) DfEnKF, (b, e, h), 3DVar, and (c, f, i) HEn3DVar50%B, respectively.